



Vorticity effects on steady nonlinear periodic gravity-capillary waves in finite depth

S. Halder, M. Francius, A.K. Dhar, S. Mukherjee, H.C. Hsu and C. Kharif

(Received 18 July 2024; revised 23 February 2025; accepted 11 March 2025)

Periodic gravity-capillary waves on a fluid of finite depth with constant vorticity are studied theoretically and numerically. The classical Stokes expansion method is applied to obtain the wave profile and the interior flow up to the fourth order of approximation, which thereby extends the works of Barakat & Houston (1968) J. Geophys. Res. 73 (20), 6545–6554 and Hsu et al. (2016) Proc. R. Soc. Lond. A 472, 20160363. The classical perturbation scheme possesses singularities for certain wavenumbers, whose variations with depth are shown to be affected by the vorticity. This analysis also reveals that for any given value of the physical depth, there exists a threshold value of the vorticity above which there are no singularities in the theoretical solution. The validity of the third- and fourth-order solutions is examined by comparison with exact numerical results, which are obtained with a method based on conformal mapping and Fourier series expansions of the wave surface. The outcomes of this comparison are surprising as they report important differences in the internal flow structure, when compared with the third-order predictions, even though both approximations predict almost perfectly the phase velocity and the surface profiles. Usually, this occurs when the wavenumber is far enough from a critical value and the steepness is not too large. In these non-resonant cases, it is found that the fourth-order theory is more consistent with the exact numerical results. With negative vorticity the improvement is noticeable both beneath the crest and the trough, whereas with positive vorticity the fourth-order theory does a better job either beneath the crest or beneath the trough, depending of the type of the wave.

¹Department of Mathematics, Indian Institute of Engineering Science and Technology, Shibpur, Howrah, West Bengal 711103, India

²Université de Toulon, Aix Marseille Université, CNRS, IRD, MIO, Toulon, France

³Department of Marine Environment and Engineering, National Sun Yat-Sen University, Kaohsiung, 804, Taiwan

⁴CNRS, Centrale Marseille, IRPHE, UMR 7342, Aix-Marseille Université Marseille 13384, France **Corresponding author**: M. Francius, marc.francius@mio.osupytheas.fr

Key words: capillary waves

1. Introduction

Gravity-capillary (GC) waves can propagate at the surface of a fluid when both gravity and surface tension are important as restoring forces. Usually, they first appear during the initial generation of waves by the wind, but they may also result from almost breaking gravity waves, rain or other millimetric- to centimetric-sized disturbances.

In view of their importance to wave energy transfer across the spectrum due to nonlinear wave—wave interactions, and to air—sea momentum transfer as they contribute to some extent to the ocean surface stress, and to remote sensing of the ocean surface as their wavelengths (from 2 mm to 2 dm) contribute to a large extent to the sea-surface backscattering of electromagnetic microwaves in the X-band (centimetre range) and the Ku-band (subcentimetre range), they have been the subject of many studies. In fact, understanding their properties has been of utmost importance during the last decades with the advances of imaging airborne and spaceborne radars. The present investigation, however, is restricted to the problem of periodic GC waves steadily travelling on water of finite depth with a linear shear current.

Generally, methods used to solve problems related to periodic GC waves of arbitrary amplitude can be divided in two main types. One is based on perturbation expansion methods and the second category is purely numerical. The first to investigate GC waves was Harrison (1909) who obtained a third-order Stokes-type solution to the problem of periodic GC waves steadily travelling on water of infinite depth in irrotational flows. This work was extended to fifth order by Wilton (1915), who also found that the classical Stokes expansion method breaks down for a countable set of critical wavenumbers. For the largest of these critical wavenumbers Wilton showed that two different solutions could exist, the so-called Wilton ripples. One of the profiles is gravity-like having a phase speed that increases with the amplitude, while the other is capillary-like having a phase speed that decreases as the amplitude increases. The phenomenon of Wilton's ripples was further analysed by Pierson & Fife (1961) and Nayfeh (1970b), who found valid solutions when the wavenumber is near the first critical value and second critical value, respectively.

These works based on perturbation expansions culminated in the higher-order extensions by computer with the seminal reference works of Hogan (1980, 1981), using the methods pioneered by Schwartz (1974) for gravity waves. On extending Pierson & Fife (1961), the phenomenon of Wilton's ripples was resolved by Hogan (1981), who showed how to modify the perturbation scheme to avoid the non-uniformity in the ordering of the Fourier coefficients of the surface profile, which occurs when the wavenumber is both at and near singular values. In finite depth the classical perturbation method was carried out by Nayfeh (1970a) and Barakat & Houston (1968) to third and fourth order, respectively. Wilton ripples were also found to exist in finite depth, and Wilton-like solutions were derived at second order by Barakat & Houston (1968) and at third order by Nayfeh (1970a).

Though much attention has been given to GC waves at the free surface of irrotational flows, rather few studies have been made in the case when the flow is rotational. While irrotational flows are suitable for waves travelling into still water or over a uniform current, non-uniform currents usually give rise to water flows with vorticity. Quite apart from the difficult questions of existence, uniqueness and analyticity of small amplitude GC waves in the case of a rotational flow with finite depth (readers interested by these issues may read Martin (2013), Martin & Matioc (2013) and references therein), a brief, and certainly incomplete, review of the literature shows that the vast majority of existing works

concerning GC waves on rotational currents assume that the waves are two-dimensional and the background current is linearly varying with depth, as these assumptions simplify the analysis, and thus the flows have constant vorticity.

In contrast with the case when surface tension is neglected, studies devoted to the computations of travelling periodic GC waves in the presence of a linear sheared current are very limited. One can refer to the paper by Brantenberg & Brevik (1993) who used a two-layer model for the background current, the constant vorticity being confined in an upper layer on top of an infinite irrotational layer, and a third-order Stokes expansion for the GC waves propagating on the surface of the upper layer. Subsequently, Hsu *et al.* (2016) derived a third-order Stokes-like solution for periodic steady waves which includes the effects of capillarity and constant vorticity, assuming a single layer model.

Using numerical methods, inclusion of surface tension effects in rotational flows with constant vorticity has also been considered by Kang & Vanden-Broeck (2000), but the focus was more on pure solitary waves and the so-called generalized solitary waves that are characterized by oscillatory tails in the far field. Most recently, in the same vein, Guo *et al.* (2014) have carried out numerical studies on the unsteady dynamics of GC solitary waves, using the same time-dependent conformal mapping technique introduced by Choi (2009) for pure gravity waves in a background linear sheared current.

Recently, there has been a renewed interest in several aspects of the dynamics of GC waves in the case of constant vorticity and finite depth. Following Chabane & Choi (2019) who analysed, for irrotational flows, the interactions of three distinct GC modes that are not necessarily collinear, Ivanov & Martin (2019) derived the amplitude equations to study three-wave resonant interactions of one-directional propagating GC waves in the presence of a linear sheared current. Moreover, from multiple scale expansion of the primitive equations in finite depth and classical expansions series of the unknown variables, Hsu et al. (2018) derived a third-order nonlinear Schrödinger equation to study the stability of weakly nonlinear uniform GC wavetrain to one-dimensional disturbances. By analysing the effect of vorticity on the stability diagrams of the problem, Hsu et al. (2018) concluded that the properties of modulational instabilities (side-band disturbances) of a uniform GC wavetrain depend crucially on the existence of a linear shear current. At the same time, Curtis et al. (2018) derived a higher-order nonlinear Schrödinger equation in the presence of surface tension, to further investigate how a linearly sheared current affects the modulational instability properties of weakly nonlinear GC waves in deep water, with a particular attention on the motion and mean properties of particle paths. Later on, Dhar & Kirby (2023) extended the results of Hsu et al. (2018) to fourth order in the finite depth case, and they showed that their results exhibit considerable deviations from those obtained with the third-order analysis. Very recently, in order to get insights in the modulational instabilities, Gao et al. (2021) have developed weakly nonlinear theories for two particular resonant cases, second-harmonic resonance and long-wave-short-wave interaction between capillary-gravity waves in finite depth with a linear shear current. We should also mention that the modulational instability has also been studied from heuristic non-local evolution equations with both surface tension and constant vorticity, more precisely with an extension of the heuristic Whitham equation by Hur & Johnson (2015) and with a corresponding set of shallow water equations by Hur (2019) to permit bidirectional propagation.

Considering the results mentioned above and given that, to the best of the authors' knowledge, all the existing Stokes-type solutions for GC waves with constant vorticity in finite depth are only accurate up to the third order, we shall extend in this paper the analysis of Hsu *et al.* (2016) to include the fourth-order effects. The present paper also extends the work of Barakat & Houston (1968) who obtained, without vorticity, the fourth-order Stokes-like solutions for periodic GC waves in finite depth. One source

of motivation in the present study has been the discovery by Fang *et al.* (2023) that experimental evidences indicate that higher-order Stokes solutions are more accurate in describing the velocity distributions, especially in strong following currents and positive vorticity conditions. These authors have derived a new set of fifth-order Stokes solutions for periodic gravity-waves interacting with a linear shear current.

To assess the accuracy of the third- and fourth-order theories, we shall obtain the reference solution of the primitive equations using a numerical method based on a conformal mapping method and Fourier series expansions of the unknowns. The differences between the exact results and the approximations are examined in terms of surface profile, phase velocity and interior horizontal wave-induced velocities. It should be emphasized that, with constant vorticity and surface tension effects taken into account, previous studies based on perturbation methods have focused mainly on the wave profiles, but rarely on the wave-induced velocities beneath the free surface. As far as we know, only Curtis *et al.* (2018) have used a second-order approximation of the interior wave-induced velocities in infinite depth, in order to analyse the mean transport properties of weakly modulated plane GC waves with constant vorticity. Thus, our work complements the work of Curtis *et al.* (2018), and reveals that significant differences between the third-order and fourth-order predictions exist in the wave-induced velocities below the free surface, even though both approximations predict almost perfectly the phase velocity and the surface profiles.

The paper is organized as follows. The basic equations and the framework of the problem is presented in § 2. In § 3, we derive the fourth-order analytical solution for these periodic GC waves and discuss the effects of depth and vorticity on the occurrence of singularities in the classical perturbation theory. In contrast with the analysis presented by Hsu *et al.* (2016) the occurrence of singularities at any order is unambiguously elucidated as a function of depth and vorticity. In § 4, we first introduce a numerical method to compute exact steady GC wave solutions with constant vorticity in finite depth and, following, a comparison between the numerical results and the analytical results is presented. Final remarks are summarized in § 5.

2. Basic equations for steady waves

As is well known for two-dimensional incompressible flows of inviscid fluids, any perturbations of a background flow with constant vorticity, either small or of finite amplitude, are necessarily irrotational motions as a consequence of Kelvin's circulation theorem. Hence, letting Ω_0 be the magnitude of the shear, it is possible to assume the existence of a velocity potential function $\Phi^*(x, y, t)$ such that the total velocity can be written as

$$\mathbf{V} = [\Omega_0(y + h_0)]\mathbf{i} + \nabla \Phi^*(x, y, t). \tag{2.1}$$

With this decomposition, the vorticity of the flow equals $-\Omega_0$. In this study, we consider the evolution of a steadily travelling periodic GC wave on the free surface of water of finite depth h_0 . The undisturbed free surface is taken to the plane y=0, where y points vertically upwards, and the bed of the water is defined by $y=-h_0$.

Dimensionless variables are introduced by the following transformations:

$$\sqrt{\frac{k_0^3}{g}} \Phi^* \to \Phi, \quad k_0 \mathbf{x} \to x, \quad \sqrt{gk_0} t \to t, \quad \frac{k_0}{\rho g} P_0 \to P, \quad \sqrt{\frac{k_0}{g}} C_* \to c, \tag{2.2}$$

where $\mathbf{x} = (x, y)$ and ρ , g, P_0 , k_0 , C_* , represent, respectively, the fluid density, gravitational acceleration, dimensional pressure, wavenumber and wave phase velocity of a steadily travelling wave. With this scaling, the relevant dimensionless parameters are

$$\Omega = \frac{\Omega_0}{\sqrt{gk_0}}, \quad \kappa = \frac{Tk_0^2}{\rho g}, \quad \mu = k_0 h_0, \tag{2.3}$$

where T represents the surface tension coefficient, and (2.1) can be expressed as

$$\mathbf{V} = [\Omega(y + \mu)]\mathbf{i} + \nabla \Phi(x, y, t). \tag{2.4}$$

Since the wave-induced motions are irrotational, the velocity potential $\Phi(x, y, t)$ satisfies the Laplace equation

$$\Phi_{xx} + \Phi_{yy} = 0$$
 for $-\mu \leqslant y \leqslant \zeta(x, t)$ (2.5)

where $y = \zeta(x, t)$ represents the dimensionless surface elevation, and the boundary conditions are

$$\Phi_{y} = 0 \quad \text{at} \quad y = -h, \tag{2.6}$$

$$\Phi_y = \zeta_t + [\Phi_x + \Omega(\zeta + \mu)]\zeta_x \quad \text{at} \quad y = \zeta(x, t),$$
 (2.7)

$$\Phi_{t} + \frac{1}{2} [\Phi_{x} + \Omega(\zeta + \mu)]^{2} + \frac{1}{2} \Phi_{y}^{2} + \zeta - \Omega \psi - \frac{\Omega^{2}}{2} (\zeta + \mu)^{2} - \kappa \zeta_{xx} (1 + \zeta_{x}^{2})^{-3/2} = f(t) \quad \text{at} \quad y = \zeta(x, t).$$
(2.8)

Here ψ is the harmonic conjugate function of Φ , and f(t) is an arbitrary function of time t, which can be set to zero without loss of generality or absorbed into the definition of Φ .

To seek steadily travelling waves of the above equations, it is also convenient to choose a frame of reference moving with the dimensionless phase velocity c. Hence, we make the following change of variables:

$$\xi = x - ct, \quad \eta = y, \quad \tau = t, \tag{2.9}$$

so that the governing equations become

$$\Phi_{\xi\xi} + \Phi_{\eta\eta} = 0, \quad -\mu \leqslant \eta \leqslant E(\xi), \tag{2.10}$$

$$\Phi_{\eta} = (\Phi_{\xi} + \Omega E - C) E_{\xi}, \quad \eta = E(\xi),$$
(2.11)

$$(\Phi_{\xi} + \Omega E - C)^2 - C^2 + \Phi_{\eta}^2 + 2E$$

$$-2\kappa E_{\xi\xi}(1+E_{\xi}^{2})^{-3/2} = K, \quad \eta = E(\xi), \tag{2.12}$$

$$\Phi_{\eta} = 0, \quad \eta = -\mu, \tag{2.13}$$

where $\Phi(\xi, \eta) = \Phi(x, y, t)$, $E(\xi) = \zeta(x, t)$, the Bernoulli's constant $K = 2\Omega\psi + \Omega^2 E^2 - 2\Omega\{E(c - \Omega\mu)\}$ and $C = c - \Omega\mu$.

3. Asymptotic solutions

In order to solve (2.10)–(2.13), we use the classical Stokes expansion method and take $\epsilon = k_0 a_1$ as a small parameter, where a_1 represents the amplitude of the first harmonic. Like Hsu *et al.* (2016), we consider the following expansions for the unknown quantities $\Phi(\xi, \eta)$, $E(\xi)$, C and K:

$$\Phi(\xi, \eta) = \sum_{m=1}^{\infty} \Phi_m(\xi, \eta), \quad E(\xi) = \sum_{m=1}^{\infty} E_m(\xi), \quad C = \sum_{m=0}^{\infty} \epsilon^m C_m, \quad K = \sum_{m=0}^{\infty} K_m,$$
(3.1)

where the quantities Φ_m , E_m and K_m are assumed to be of order ϵ^m . By definition, the quantities C_m do not depend on ϵ and so the leading-order term is m = 0, whereas each

term in the series of the velocity potential $\Phi(\xi, \eta)$ and the surface elevation amplitude $E(\xi)$ depend on the amplitude parameter ϵ , the subscript indicating its order. Substituting (3.1) in the system of equations (2.10)–(2.13) and then equating coefficients of different powers of ϵ on both sides, we obtain the approximations for consecutive orders of the nonlinear problem.

To the first order in the expansion parameter ϵ , we obtain the velocity potential and the surface elevation,

$$\Phi_1(\xi, \eta) = \frac{C_0 \epsilon}{\sigma} \frac{\cosh[(\eta + \mu)]}{\cosh(\mu)} \sin(\xi), \tag{3.2}$$

$$E_1(\xi) = \epsilon \cos(\xi), \tag{3.3}$$

$$K_1 = 0, (3.4)$$

as well as the linear dispersion relation connecting frequency and wavenumber of the primary wave

$$C_0^2 + \sigma C_0 \Omega = \sigma (1 + \kappa), \tag{3.5}$$

where $\sigma = \tanh(k_0h_0)$. Equation (3.5) is the same as equation (3.7) of Hsu *et al.* (2016) and equation (38a) of Kang & Vanden-Broeck (2000) by returning to dimensional form. Setting $\overline{\Omega} = \sigma \Omega / C_0$, the linear dispersion relation (3.5) can be rewritten like

$$C_0^2(1+\overline{\Omega}) = \sigma(1+\kappa), \tag{3.6}$$

which shows that in any case $\overline{\Omega} > -1$. As we shall see, using $\overline{\Omega}$ and $\overline{\kappa} = \kappa/(\sigma C_0^2)$, introduced for convenience, we have obtained compact formulae for the higher-order coefficients.

Calculation of the higher orders is quite standard and therefore omitted here to improve readability. The analytical work was done with Mathematica. In the following we present only the novel fourth-order equations and corresponding solutions. Since we have found few misprints in some formulae of Hsu *et al.* (2016), both at second order and third order, the intermediate results are given in appendices A and B.

Next, we discuss the occurrence of resonant cases taking into account vorticity and finite depth effects. Notice that the misprints found in the formulae of Hsu et~al.~(2016) have no consequences on the expressions of the first two critical values κ_1 and κ_2 (see appendices A and B). Actually their expressions are identical to ours, when their (B,X) are replaced by our $(\overline{\kappa},\overline{\Omega})$. When $\kappa=\kappa_1$, the second-order solutions and the third-order solutions are found to be singular, whereas when $\kappa=\kappa_2$ singularities occur only at third order. Hsu et~al.~(2016) have discussed the dependency of these critical values on depth and vorticity, but their interpretation is ambiguous. We shall therefore clarify this discussion herein this study.

3.1. Approximate solution of the fourth order

To the fourth order in ϵ , we obtain the sequence of equations given by

$$\begin{split} &\Phi_{4\xi\xi} + \Phi_{4\eta\eta} = 0, \quad -\mu \leqslant \eta < 0, \\ &\Phi_{4\eta} + C_0 E_{4\xi} = -E_1 \Phi_{3\eta\eta} - E_2 \Phi_{2\eta\eta} - E_3 \Phi_{1\eta\eta} - \frac{1}{2} E_1^2 \Phi_{2\eta\eta\eta} - E_1 E_2 \Phi_{1\eta\eta\eta} \\ &- \frac{1}{6} E_1^3 \Phi_{1\eta\eta\eta\eta} + (\Phi_{1\xi} + \Omega E_1) E_{3\xi} + (\Phi_{2\xi} + E_1 \Phi_{1\xi\eta} + \Omega E_2 - C_2) E_{2\xi}, \\ &+ (\Phi_{3\xi} + E_1 \Phi_{2\xi\eta} + E_2 \Phi_{1\xi\eta} + \frac{1}{2} E_1^2 \Phi_{1\xi\eta\eta} + \Omega E_3 - C_3) E_{1\xi}, \quad \eta = 0 \end{split} \tag{3.8}$$

$$C_{0}\Phi_{4\xi} - (1 - C_{0}\Omega)E_{4} + \kappa E_{4\xi\xi} = \frac{1}{2} \left(\Phi_{2\xi}^{2} + \Phi_{2\eta}^{2} \right) + \Phi_{1\xi}\Phi_{3\xi} + \Phi_{1\eta}\Phi_{3\eta}$$

$$+ E_{1}(\Phi_{1\xi}\Phi_{2\xi\eta} + \Phi_{2\xi}\Phi_{1\xi\eta} + \Phi_{1\eta}\Phi_{2\eta\eta} + \Phi_{2\eta}\Phi_{1\eta\eta}) + \frac{1}{2}E_{1}^{2} \left(\Phi_{1\xi\eta}^{2} + \Phi_{1\xi}\Phi_{1\xi\eta\eta} + \Phi_{1\eta\eta\eta} \right) + E_{2}(\Phi_{1\xi}\Phi_{1\xi\eta} + \Phi_{1\eta}\Phi_{1\eta\eta}) + \frac{1}{2}\Omega^{2} \left(E_{2}^{2} + 2E_{1}E_{3} \right)$$

$$+ \Omega \left(E_{1}\Phi_{3\xi} + E_{2}\Phi_{2\xi} + E_{3}\Phi_{1\xi} + E_{1}^{2}\Phi_{2\xi\eta} + 2E_{1}E_{2}\Phi_{1\xi\eta} + \frac{1}{2}E_{1}^{3}\Phi_{1\xi\eta\eta} \right)$$

$$- C_{0} \left(E_{1}\Phi_{3\xi\eta} + E_{2}\Phi_{2\xi\eta} + E_{3}\Phi_{1\xi\eta} + \frac{1}{2}E_{1}^{2}\Phi_{2\xi\eta\eta} + E_{1}E_{2}\Phi_{1\xi\eta\eta} + \frac{1}{6}E_{1}^{3}\Phi_{1\xi\eta\eta\eta} \right)$$

$$- C_{3} \left(\Phi_{1\xi} + \Omega E_{1} \right) - C_{2} \left(\Phi_{2\xi} + \Omega E_{2} + E_{1}\Phi_{1\xi\eta} \right) + \frac{3}{2}\kappa E_{1\xi}^{2}E_{2\xi\xi}$$

$$+ 3\kappa E_{1\xi}E_{2\xi}E_{1\xi\xi} - \frac{1}{2}K_{4} = 0, \quad \eta = 0, \qquad (3.9)$$

$$\Phi_{4\eta} = 0, \quad \eta = -\mu. \qquad (3.10)$$

Classically, we seek the solutions for the fourth-order potential and elevation amplitude in the form

$$\Phi_4(\xi, \eta) = A_{44} \frac{\cosh[4(\eta + \mu)]}{\cosh(4\mu)} \sin(4\xi) + A_{42} \frac{\cosh[2(\eta + \mu)]}{\cosh(2\mu)} \sin(2\xi), \qquad (3.11)$$

$$E_4(\xi) = a_{44} \cos(4\xi) + a_{42} \cos(2\xi). \qquad (3.12)$$

Then by inserting (3.11)–(3.12) into the boundary conditions (3.8)–(3.9) and using the first-, second- and third-order solutions, after tedious algebra we obtain

$$\begin{split} A_{44} &= \frac{3\epsilon}{8\left[(5+\sigma^2)-15\overline{\kappa}(1+\sigma^2)\right]} \frac{(1+6\sigma^2+\sigma^4)}{\sigma^3(1+3\sigma^2)} \left[(1+3\sigma^2)\overline{\Omega} + 2(1-3\sigma^2-2\sigma^4) \right. \\ &+ 15\overline{\kappa}\sigma^2(1+3\sigma^2) \right] A_{33} + \frac{C_0\epsilon}{8\left[(5+\sigma^2)-15\overline{\kappa}(1+\sigma^2)\right]} \frac{(1+6\sigma^2+\sigma^4)}{\sigma^4} \\ &\times \left[\overline{\Omega}^2 + \left\{2+15\overline{\kappa}\sigma^2\right\} \overline{\Omega} + (1-\sigma^2)+15\overline{\kappa}\sigma^2 \right] a_{33} \\ &+ \frac{C_0\epsilon^4}{768(1-3\overline{\kappa})^2 \left[(5+\sigma^2)-15\overline{\kappa}(1+\sigma^2)\right]} \frac{(1+6\sigma^2+\sigma^4)}{\sigma^{10}} \\ &\times \left[3\overline{\Omega}^6 + \left\{3(9+4\sigma^2)+45\overline{\kappa}\sigma^2\right\} \overline{\Omega}^5 + \left\{12(9+3\sigma^2+\sigma^4)+18\overline{\kappa}\sigma^2(21+11\sigma^2)\right\} \overline{\Omega}^4 \right. \\ &+ \left\{3(81-14\sigma^2+21\sigma^4)+9\overline{\kappa}\sigma^2(149+68\sigma^2+19\sigma^4)+270\overline{\kappa}^2\sigma^4(1+\sigma^2)\right\} \overline{\Omega}^3 \\ &+ \left\{12(27-29\sigma^2+21\sigma^4-4\sigma^6)+18\overline{\kappa}\sigma^2(139+18\sigma^2+41\sigma^4) \right. \\ &+ 27\overline{\kappa}^2\sigma^4(51-34\sigma^2+11\sigma^4)\right\} \overline{\Omega}^2 + \left\{3(81-192\sigma^2+169\sigma^4-82\sigma^6)+9\overline{\kappa}\sigma^2 \right. \\ &\times (273-110\sigma^2+253\sigma^4-12\sigma^6)+54\overline{\kappa}^2\sigma^4(47-84\sigma^2+15\sigma^4)-3240\overline{\kappa}^3\sigma^8\right\} \overline{\Omega} \\ &+ (81-342\sigma^2+432\sigma^4-302\sigma^6+131\sigma^8)+6\overline{\kappa}\sigma^2(171-177\sigma^2+359\sigma^4-283\sigma^6) \\ &+ 144\overline{\kappa}^2\sigma^4(12-38\sigma^2+43\sigma^4)-5940\overline{\kappa}^3\sigma^8 \right], \end{split}$$

$$A_{42} = \frac{3\epsilon}{4(1 - 3\bar{\kappa})} \frac{(1 + \sigma^2)}{\sigma^3(1 + 3\sigma^2)} \left[(1 + 3\sigma^2) \overline{\Omega} + 2(1 - \sigma^4) + 3\bar{\kappa}\sigma^2(1 + 3\sigma^2) \right] A_{33}$$

$$+ \frac{\epsilon}{4(1 - 3\bar{\kappa})} \frac{(1 + \sigma^2)}{\sigma^3} \left[\overline{\Omega} + 2(1 - \sigma^2) + 3\sigma^2 \overline{\kappa} \right] A_{31} - \frac{\epsilon^4}{8(1 - 3\bar{\kappa})^2} \frac{(1 + \sigma^2)}{\sigma^6}$$

$$\times \left[\overline{\Omega}^3 + \left\{ (5 + 2\sigma^2) + 3\bar{\kappa}\sigma^2 \right\} \overline{\Omega}^2 + \left\{ 3(3 + \sigma^2) + 6\bar{\kappa}\sigma^2(2 + \sigma^2) \right\} \overline{\Omega}$$

$$+ (6 - \sigma^2 - \sigma^4) + 3\bar{\kappa}\sigma^2(5 - \sigma^2) \right] C_2 + \frac{C_0 \epsilon^4}{48(1 - 3\bar{\kappa})^2} \frac{(1 + \sigma^2)}{\sigma^6} \left[18\bar{\Omega}^3 + \left\{ 3(25 + \sigma^2) + 45\bar{\kappa}\sigma^2 \right\} \overline{\Omega}^2 + \left\{ 39(3 - \sigma^2) + 18\bar{\kappa}\sigma^2(7 - \sigma^2) + 54\bar{\kappa}^2\sigma^4 \right\} \overline{\Omega}$$

$$+ (63 - 52\sigma^2 + 13\sigma^4) + 3\bar{\kappa}\sigma^2(31 - 23\sigma^2) + 90\bar{\kappa}^2\sigma^4 \right], \qquad (3.14)$$

$$a_{44} = \frac{\tanh(4\mu)}{C_0} A_{44} + \frac{3\epsilon}{2C_0} A_{33} + \frac{\epsilon}{2\sigma} (\overline{\Omega} + 1) a_{33} + \frac{\epsilon^4}{192(1 - 3\bar{\kappa})^2} \frac{1}{\sigma^7}$$

$$\times \left[3\bar{\Omega}^5 + 12(2 + \sigma^2)\bar{\Omega}^4 + \left\{ 9(9 + 6\sigma^2 + \sigma^4) + 18\bar{\kappa}\sigma^2(1 + \sigma^2) \right\} \overline{\Omega}^3 + \left\{ 12(12 + 7\sigma^2 + 2\sigma^4) + 18\bar{\kappa}\sigma^2(5 + \sigma^4) \right\} \overline{\Omega}^2 + \left\{ 3(45 + 12\sigma^2 + 13\sigma^4 - 2\sigma^6) + 18\bar{\kappa}\sigma^2(9 - 8\sigma^2 + 3\sigma^4) - 216\bar{\kappa}^2\sigma^6 \right\} \overline{\Omega} + 2(27 - 9\sigma^2 + 27\sigma^4 - 31\sigma^6) + 12\bar{\kappa}\sigma^2(9 - 21\sigma^2 + 28\sigma^4) - 396\bar{\kappa}^2\sigma^6 \right], \qquad (3.15)$$

and, furthermore,

$$a_{42} = \frac{\tanh(2\mu)}{C_0} A_{42} + \frac{3\epsilon}{2C_0} A_{33} + \frac{\epsilon}{2C_0} A_{31} - \frac{\epsilon^2}{C_0} (C_2 a_2) + \frac{\epsilon^4}{24(1 - 3\overline{\kappa})} \frac{1}{\sigma^3}$$

$$\times \left[9\overline{\Omega}^2 + \left\{ 3(9 + \sigma^2) + 18\overline{\kappa}\sigma^2 \right\} \overline{\Omega} + (27 - 19\sigma^2) + 30\overline{\kappa}\sigma^2 \right], \qquad (3.16)$$

$$K_4 = \frac{C_0 \epsilon}{\sigma} (\overline{\Omega} + 1) A_{31} + \frac{C_0^2 \epsilon}{\sigma^2} (\overline{\Omega}^2 + \overline{\Omega} - \sigma^2) a_{31} - \epsilon^4 C_0 C_2 + \frac{C_0^2 \epsilon^4}{32(1 - 3\overline{\kappa})^2} \frac{1}{\sigma^8}$$

$$\times \left[\overline{\Omega}^6 + 4(2 + \sigma^2) \overline{\Omega}^5 + \left\{ 4(7 + 4\sigma^2 + \sigma^4) + 6\overline{\kappa}\sigma^2 (1 + \sigma^2) \right\} \overline{\Omega}^4 + \left\{ 2(27 + 8\sigma^2 + 9\sigma^4) + 12\overline{\kappa}\sigma^2 (3 - 2\sigma^2 + \sigma^4) \right\} \overline{\Omega}^3$$

$$+ \left\{ 12(5 - 2\sigma^2 + 5\sigma^4) + 12\overline{\kappa}\sigma^2 (7 - 14\sigma^2 + 2\sigma^4) + 9\overline{\kappa}^2\sigma^4 (1 - 10\sigma^2 + \sigma^4) \right\} \overline{\Omega}^2$$

$$+ \left\{ 12(3 - 5\sigma^2 + 9\sigma^4 - 2\sigma^6) + 6\overline{\kappa}\sigma^2 (15 - 53\sigma^2 + 27\sigma^4 - \sigma^6) + 36\overline{\kappa}^2\sigma^4 (1 - 6\sigma^2) \right\}$$

$$\times \overline{\Omega} + (9 - 36\sigma^2 + 78\sigma^4 - 40\sigma^6 + 9\sigma^8) + 12\overline{\kappa}\sigma^2 (3 - 15\sigma^2 + 12\sigma^4 - 4\sigma^6)$$

$$+ 36\overline{\kappa}^2 \sigma^4 (1 - 9\sigma^2 + 2\sigma^4) \right], \qquad (3.17)$$

$$C_3 = 0. \qquad (3.18)$$

Equations (3.13)–(3.18) constitute the main analytical results of this study and extend the third-order analysis initiated by Hsu *et al.* (2016). In the next section we shall use these relations to describe the improvements gained with the fourth-order approximation by analysing not only the surface profiles but also the internal flow velocities.

Not surprisingly, the fourth-order approximation is found to be invalid when κ equals another critical value, κ_3 , the root of the following equation:

$$\kappa = \frac{(5+\sigma^2)\sigma^2}{15(1+\overline{\Omega}) + 5(2+3\overline{\Omega})\sigma^2 - \sigma^4}.$$
 (3.19)

Without vorticity, (3.19) becomes

$$\kappa_3 = \frac{(5+\sigma^2)\sigma^2}{15+10\sigma^2-\sigma^4} \tag{3.20}$$

in agreement with the results of Barakat & Houston (1968). This latter equation reduces in deep water ($\sigma = 1$) to the other well-known value $\kappa_3 = 1/4$.

3.2. Critical wavenumbers

Since the pioneering works of Harrison (1909) and Pierson & Fife (1961), it is well known that the application of the Stokes expansion method for the periodic steady irrotational GC wave problem, either in deep water or finite depth, is not legitimate when κ is close to the critical values κ_n ($n \ge 1$), which form, when they exist, an infinite discrete set of critical values. At these critical values, it is observed that there is a lack of uniqueness in the linear solution. Physically, it can be explained by a resonance mechanism due to the fact that infinitesimal waves of wavenumber k_0 and nk_0 have the same phase velocity when $\kappa = \kappa_n$.

For irrotational GC waves on finite depth, Barakat & Houston (1968) remarked that the *n*th approximation obtained with the classical Stokes expansion method breaks down when $\kappa = \kappa_{n-1}$, the roots of the following equations:

$$\kappa = \frac{n \tanh \mu - \tanh(n\mu)}{n^2 \tanh(n\mu) - n \tanh \mu}, \qquad n \geqslant 2.$$
 (3.21)

In deep water these roots have the well-known values $\kappa_{n-1} = 1/n$ ($n \ge 2$). Solutions that bifurcate from these critical values are the so-called Wilton ripples, which correspond to resonances between the fundamental and the nth harmonic. For n = 4, with some algebra one can show that (3.21) corresponds to (3.20).

If the dependence between the dimensionless parameters κ and μ is not considered, graphs of κ_n versus μ may be misleading with respect to the interpretation of the influence of the depth of the fluid layer. It should be realized that the critical numbers are the roots κ_{n-1} of the following equations for $n \geqslant 2$:

$$\kappa \left[n^2 \tanh(n\kappa^{1/2}\tilde{h}) - n \tanh(\kappa^{1/2}\tilde{h}) \right] - \left[n \tanh(\kappa^{1/2}\tilde{h}) - \tanh(n\kappa^{1/2}\tilde{h}) \right] = 0, \quad (3.22)$$

obtained from (3.21) and the relation $\mu = \kappa^{1/2} \tilde{h}$, where $\tilde{h} = k_c h_0$ and $k_c = \sqrt{\rho g/T}$. Numerical calculations were performed for water (T=74 dynes cm⁻¹), by using a variant of the Newton–Raphson method to solve (3.22) for κ . The results for the first three critical values are shown in figure 1 as a function of \tilde{h} . The dotted lines represent the well-known asymptotic values of κ_n (n=1,2 and 3) for irrotational GC waves in deep water. The thin solid lines are drawn to show the dependency of the dimensionless number κ on the depth layer \tilde{h} for fixed values of μ . The thin solid lines of figure 1 are drawn for $\mu=10,2$ and 1.

As shown in figure 1 the critical values κ_n decrease rapidly with decreasing \tilde{h} , and eventually disappear when $\tilde{h} < \tilde{h}_c = \sqrt{3}$. It is noticed that these results match those of figure 2 in Barakat & Houston (1968). For water $\tilde{h}_c = \sqrt{3}$ corresponds to the particular water depth $h_0 \approx 4.76$ mm. In fact, when the surface tension is large, or equivalently, the

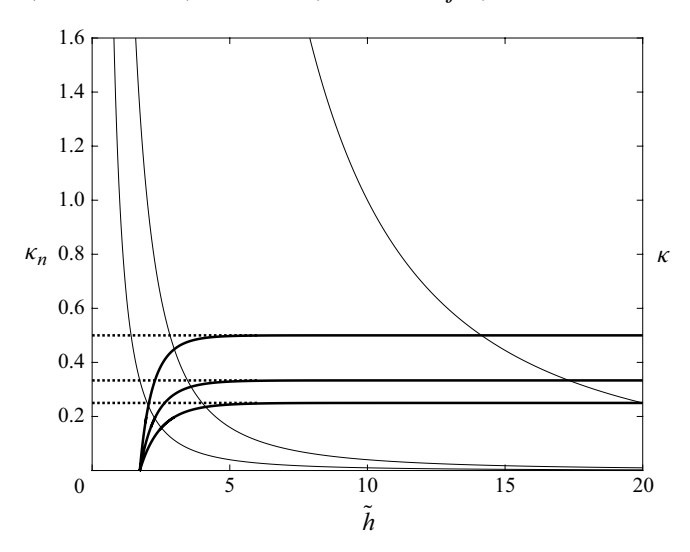


Figure 1. Variations of κ_1 , κ_2 , κ_3 as a function of depth for water for irrotational GC waves. In any case $\kappa_1 > \kappa_2 > \kappa_3$. The dotted lines represent the corresponding deep-water values. Using a separate y-axis, the relation $\mu = \kappa^{1/2} \tilde{h}$ is plotted for $\mu = 10$, 2 and 1 (from the right to the left).

fluid depth is sufficiently small so that $\tilde{h} < \tilde{h}_c$, the phase velocity is strictly a monotonic function of the wavenumber, and thus no resonances are possible. In other words, when $\tilde{h} < \tilde{h}_c$ the asymptotic expansion of the solution is regular to any order, as demonstrated by Nayfeh (1970a) who considered the limit $\mu \ll 1$. In contrast, when $\tilde{h} > \tilde{h}_c = \sqrt{3}$ resonances between the fundamental and the nth harmonic are possible. Figure 1 also indicates that using the asymptotic theory with a constant value of μ , the fundamental dimensional wavenumber k_0 being kept fixed, the first three singularities are found at the intersections between the corresponding thin solid line and the curves in thick solid lines. It should be emphasized that for a given μ each critical value of the wavenumber corresponds indeed to a different physical depth of the fluid layer. Nonetheless, for $\tilde{h} > 5$, the effects of the depth are negligible and the GC waves may be regarded as deep-water phenomena.

It is possible to generalize the approach of Barakat & Houston (1968) to the case of GC waves with constant vorticity in finite depth. Namely, for steadily travelling periodic waves it is expected that the nth-order approximation obtained with the classical Stokes expansion method will break down when the wavenumber k_0 satisfies the following relation:

$$C_*(k_0) = C_*(nk_0) \tag{3.23}$$

or equivalently in dimensionless form, considering only forward propagating modes,

$$-\frac{\Omega}{2}\alpha_1 + \sqrt{\left(\frac{\Omega\alpha_1}{2}\right)^2 + (1+\kappa)\alpha_1} = -\frac{\Omega}{2}\alpha_n + \sqrt{\left(\frac{\Omega\alpha_n}{2}\right)^2 + (1+n^2\kappa)\alpha_n}, \quad (3.24)$$

where $n\alpha_n = \tanh(n\mu)$. With elementary relations for hyperbolic functions and some algebra, it can be shown that (3.24) yields the equations (A12), (B12) and (3.19) when n=2,3 and 4 (respectively), and therefore represents the extension of (3.21) in the presence of current shear. Introducing $\tilde{\Omega} = \Omega_0/\sqrt{gk_c}$ and using the relation $\Omega = \kappa^{-1/4}\tilde{\Omega}$, one can see that (3.24) defines a nonlinear equation for κ for fixed values of the two intrinsic dimensionless parameters, \tilde{h} and $\tilde{\Omega}$. It should be emphasized here that in the

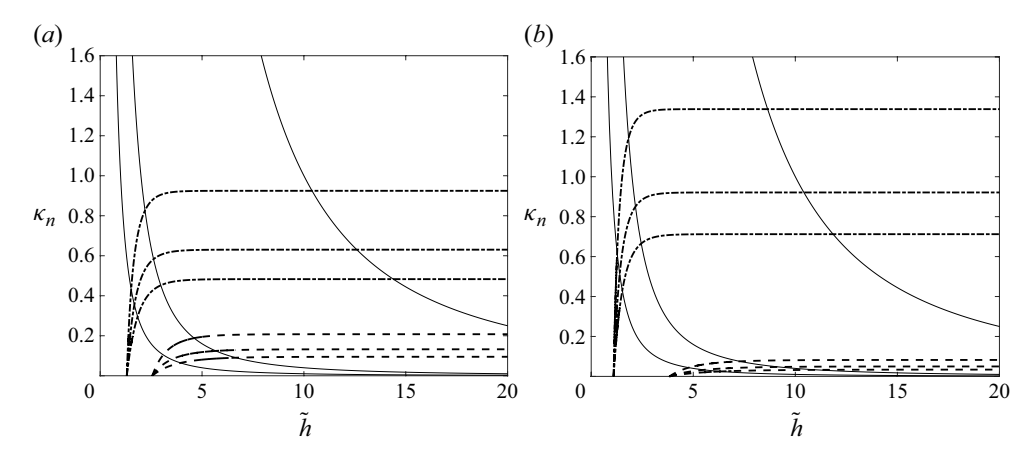


Figure 2. Variations of κ_1 , κ_2 , κ_3 as a function of depth for water for different values of the shear parameter: (a) $\tilde{\Omega} = \pm 0.5$; (b) $\tilde{\Omega} = \pm 0.9$. In any case $\kappa_1 > \kappa_2 > \kappa_3$; dashed lines correspond to positive values of $\tilde{\Omega}$, dash-dotted lines to negative ones and thin solid lines are drawn for $\mu = 10$, 2 and 1 (from the right to the left).

analysis carried out by Hsu *et al.* (2016) the fully implicit definition of the critical wavenumbers was not properly recognized. More explicitly, the relation $\Omega = \kappa^{-1/4}\tilde{\Omega}$ was not taken into account when solving for the roots of (B11) and (B12). This gives rise to ambiguous results, as for instance the doubling of the critical wavenumbers at second and third order when $\Omega < 0$ for a given fixed 'physical' dimensionless depth \tilde{h} (see figure 2 in Hsu *et al.* (2016)). Though the plotted results in figure 2 of Hsu *et al.* (2016) are correct, their interpretation may be misleading.

Numerical calculations were also performed for water (T=74 dynes/cm) to solve (3.24) for κ . The results for the first three critical values are shown in figure 2 as a function of \tilde{h} with four different values of the shear parameter $\tilde{\Omega}$. In any case it is seen that there is still a critical depth, \tilde{h}_* , below which resonances are not possible, although it depends on the value of the vorticity. When resonances are possible, namely when $\tilde{h} > \tilde{h}_*$, we always have $\kappa_1 > \kappa_2 > \kappa_3$ and their values are, of course, different from the irrotational case. Figure 2 shows that these critical values increase (decrease) with increasing positive (negative) vorticity. Interestingly, given that κ_1 decreases with increasing (negative) vorticity when $\tilde{h} > \tilde{h}_*$, the interval $[\kappa_1, \infty[$, over which the asymptotic theory is regular, also increases.

Actually the dependency of \tilde{h}_* on the shear parameter $\tilde{\Omega}$ can be analysed with the analytical results obtained by Martin (2013). As far as we are concerned with the forward propagating mode, we can use his Lemma 3 to write the appropriate relationship in dimensionless form, as

$$\tilde{h}_{*}^{2} = 3 + \tilde{\Omega}\tilde{h}_{*} \left[\tilde{h}_{*} \sqrt{\tilde{h}_{*} + \frac{\tilde{\Omega}^{2}\tilde{h}_{*}^{2}}{4}} - \frac{\tilde{\Omega}\tilde{h}_{*}}{2} \right].$$
 (3.25)

Figure 3, in which the solution of (3.25) is plotted as a function of $\tilde{\Omega}$, shows that $\tilde{h}_* > \sqrt{3}$ when $\tilde{\Omega} > 0$ and $\tilde{h}_* < \sqrt{3}$ when $\tilde{\Omega} < 0$. In the region below the solid curve plotted in this figure, namely when $\tilde{h} < \tilde{h}_*$, resonances are not possible and thus the asymptotic theory is regular for any wavenumber. Notice that Gao *et al.* (2021) have also described the effects of vorticity on the properties of the dispersion relation and obtained identical results for the forward propagating mode. Actually the first case in their inequalities (13) correspond

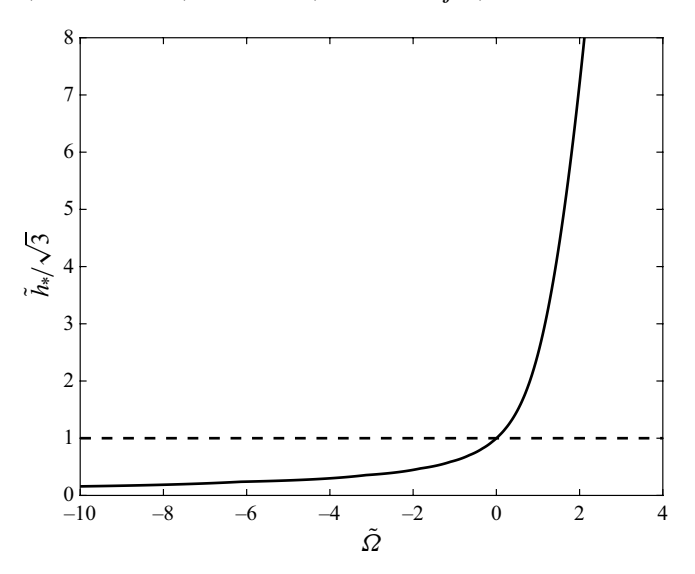


Figure 3. Normalized critical depth \tilde{h}_* as a function of $\tilde{\Omega}$.

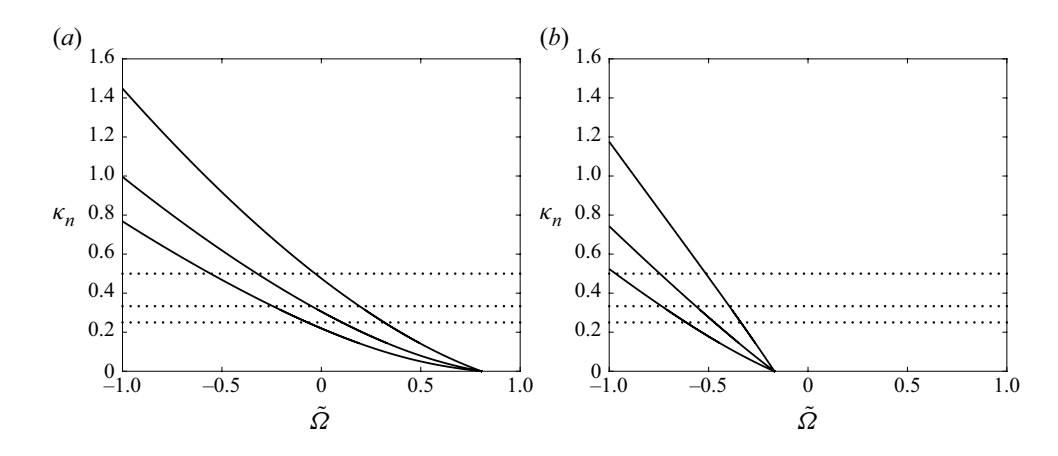


Figure 4. Variations of κ_1 , κ_2 , κ_3 for different values of \tilde{h} for water as a function of the shear parameter $\tilde{\Omega}$: (a) $\tilde{h}/\sqrt{3}=2$; (b) $\tilde{h}/\sqrt{3}=0.9$. In any case $\kappa_1>\kappa_2>\kappa_3$. The dotted lines represent the corresponding well-known values in deep water.

to the region in figure 3 where $\tilde{h} < \tilde{h}_*$, which they have named shallow-water regime. Figure 3 also reveals that for any given value of the physical depth, or equivalently \tilde{h} , there exist a threshold value of $\tilde{\Omega}$ above which there are no resonances. This particular value is positive when $\tilde{h} > \sqrt{3}$, but negative when $\tilde{h} < \sqrt{3}$. This is further illustrated in figure 4, where the critical values κ_{n-1} (n=2,3) and 4) are plotted as a function of $\tilde{\Omega}$ for two particular values of the depth.

4. Numerical results

In this section we first present the numerical method used to compute steadily travelling wave solutions of the Euler equations with surface tension and constant vorticity in finite

depth. Then, by comparison, we study the validity of the third and fourth-order solutions in two cases, namely, (i) GC waves without vorticity and (ii) GC waves on linear sheared currents.

In the most general case, a family of steadily travelling wave solutions lies on a region of a four-parameter space, which involves a quadruplet of dimensionless parameters, either $(\kappa, \mu, \Omega, \epsilon)$ or $(\kappa, \tilde{h}, \tilde{\Omega}, \epsilon)$. We shall use the former quadruplet in this section, like in the recent works of Hsu *et al.* (2018) and Dhar & Kirby (2023) concerning the stability analysis of GC waves in finite depth and constant vorticity within the framework of envelope equations. It is worth noting that with our choice of scaling the two quadruplets are equivalent only when $\kappa=1$. As explained in § 3.2, when $\kappa\neq 1$ the latter quadruplet (with $\epsilon=0$) is preferable to analyse unambiguously the effects of depth and vorticity on the occurrence of critical values of κ for the perturbation scheme.

4.1. Fully nonlinear solutions

To compute steadily travelling periodic GC waves with constant vorticity in finite depth, we shall use a numerical method based on a conformal mapping method and Fourier series expansions of the unknowns, such as given by Guo *et al.* (2014) and Choi (2009) for two-dimensional GC solitary waves and gravity waves, respectively. It is emphasized here that, though these authors established the governing equations for GC waves in finite depth with constant vorticity, the numerical computations were carried out only in the deep-water case. The formulation of the governing equations in the transformed plane (a canonical strip) is well documented by these authors, and therefore needs not to be reproduced here.

To be concise and consistent, however, we present the transformed governing equations used in our study and adopt the same notations as Ribeiro *et al.* (2017) except for the coordinates in the canonical domain. Namely the conformal map is defined as $\tilde{Z}(\zeta, \vartheta) = \tilde{X}(\zeta, \vartheta) + i\tilde{Y}(\zeta, \vartheta)$ and the surface elevation as $z = \eta(X) = Y(\zeta)$ where $X = \tilde{X}(\zeta, 0)$ and $Y = \tilde{Y}(\zeta, 0)$. After performing similar calculations as those presented in Choi (2009), we can show that the free surface kinematic and dynamic boundary conditions can be combined into a single pseudodifferential equation for the free surface elevation $Y(\zeta)$,

$$-\frac{\tilde{c}^{2}}{2} - \frac{\tilde{c}^{2}}{2J} + Y + \gamma^{2} \frac{\left(\mathcal{C}\left[\left(Y+b\right)Y_{\zeta}\right]\right) - \left(\left(Y+b\right)Y_{\zeta}\right)^{2}}{2J} - \gamma \tilde{c}b + \frac{\left(\tilde{c} + \gamma \mathcal{C}\left[\left(Y+b\right)Y_{\zeta}\right]\right)\left(\tilde{c} + \gamma \left(Y+b\right)\left(1-\mathcal{C}\left[Y_{\zeta}\right]\right)\right)}{J} + \tilde{\kappa} \frac{X_{\zeta}Y_{\zeta\zeta} - Y_{\zeta}X_{\zeta\zeta}}{J^{3/2}} = \tilde{B}, \quad (4.1)$$

where $J=\tilde{X}_{\zeta}^2+\tilde{Y}_{\zeta}^2$ is Jacobian of the conformal map evaluated at the free surface. According to our choice of scaling (see § 2), we have $\tilde{c}=C/\sqrt{\mu}$, $\tilde{\kappa}=\kappa/\mu^2$, $\gamma=-\sqrt{\mu}\Omega$, and \tilde{B} is the Bernoulli constant. As explained in Ribeiro *et al.* (2017), b is a free parameter that determines the choice of the reference frame, or equivalently the depth at which the Eulerian mean horizontal velocity is zero in the limit of small amplitude waves. Since the governing equations have the property of Galilean invariance, the parameter b affects neither the shape of the wave nor the streamlines in the frame of reference travelling with the wave. For the comparison with the analytical results derived in § 3 we shall take b=0. Equation (4.1) contains three additional unknowns, the phase velocity \tilde{c} , the Bernoulli constant \tilde{B} and the conformal depth \tilde{d} , the latter being embedded in the pseudodifferential operator C, defined as $C[f] = \mathcal{F}^{-1}[i \cot(k\tilde{d}) \hat{f}_k]$ where $\hat{f}_k = \mathcal{F}[f]$ and \mathcal{F} represents the Fourier transform operator. Accordingly, we also have the relation

$$X_{\zeta} = 1 - \mathcal{C}\left[Y_{\zeta}\right]. \tag{4.2}$$

To obtain a closed system of equations for the unknowns, (4.1) must be supplemented by three additional equations. We choose to impose a zero-mean level in the physical space,

$$\int_0^{L/2} Y X_{\zeta} \,\mathrm{d}\zeta = 0,\tag{4.3}$$

and, assuming the wave crest is at $\zeta = 0$, we fix the dimensionless wave height through

$$Y(0) - Y(L/2) = H, (4.4)$$

as well as the depth condition

$$\tilde{d} = 1 + \frac{1}{L} \int_{-L/2}^{L/2} Y d\zeta.$$
 (4.5)

A Fourier spectral discretization for the unknown function $Y(\zeta)$ allows one to obtain an efficient numerical method with fast Fourier transform, wherein all derivatives and pseudodifferential operators are calculated via Fourier multipliers while the nonlinear terms are computed pseudospectrally (with dealiasing). Hence, we consider a truncated Fourier series with N modes,

$$Y(\zeta) = \sum_{n=-N/2}^{N/2} \hat{Y}_n e^{in\frac{2\pi}{L}\zeta}, \qquad \hat{Y}_0 = 0, \tag{4.6}$$

and assume that the solutions are periodic with a wavelength $L=2\pi/\mu$ equal to the dimensionless wavelength in the physical space. Note that $\hat{Y}_{-n}=\hat{Y}_n^*$ since the surface elevation is a real function. Taking N even and considering only symmetric waves, we discretize (4.1) at N/2+1 collocation points uniformly distributed over a half-period, $\zeta_j=(j-1)L/N$ with $j=1,\ldots,N/2+1$, to obtain N/2+1 equations for the unknown values $Y_j=Y(\zeta_j),\ j=1,\ldots,N/2+1$. Performing the discretization of the additional equations, (4.3)–(4.5), we can close the system for the N/2+4 unknowns $\tilde{c},\ \tilde{B},\ \tilde{d}$ and $Y_j,\ j=1,\ldots,N/2+1$.

To solve the resulting nonlinear system of algebraic equations, we use the Levenberg–Marquardt algorithm implemented in the fsolve function of the Optimisation Toolbox of MATLAB. As an initial guess for this iterative procedure we use the first-order solution presented in § 3,

$$\tilde{c} = C_0/\mu, \qquad \tilde{B} = 0, \qquad \tilde{d} = 1, \qquad Y(\zeta) = H \cos\left(\frac{2\pi}{L}\zeta\right),$$
 (4.7)

where $H = \epsilon/\mu$ with our choice of scaling and ϵ is small. Unlike Ribeiro *et al.* (2017), who used the mean absolute residuals errors for the whole system of equations, our stopping criterion is based on the infinite norm of the residuals of (4.1). In our practice, with N = 128 or 256 both errors were found to be of the order 10^{-12} .

The following numerical results were obtained by natural numerical continuation in the parameters space, using the prior converged solution as the initial guess to a new solution. Owing to the number of dimensionless parameters characterizing branches of solutions, it is obviously a difficult task to give a thorough description of the bifurcation diagrams. Even in the simpler case of irrotational flows in deep water, namely with $\Omega=0$ and $\mu=\infty$, Shelton et~al.~(2021) have shown that the bifurcation space of the GC problem is certainly non-trivial, rendering difficult to observe any clear structure. Crucially, this is due to the existence of multiple solutions, the so-called Wilton ripples or combined waves, which emerge from resonant interactions between two modes. On account of this

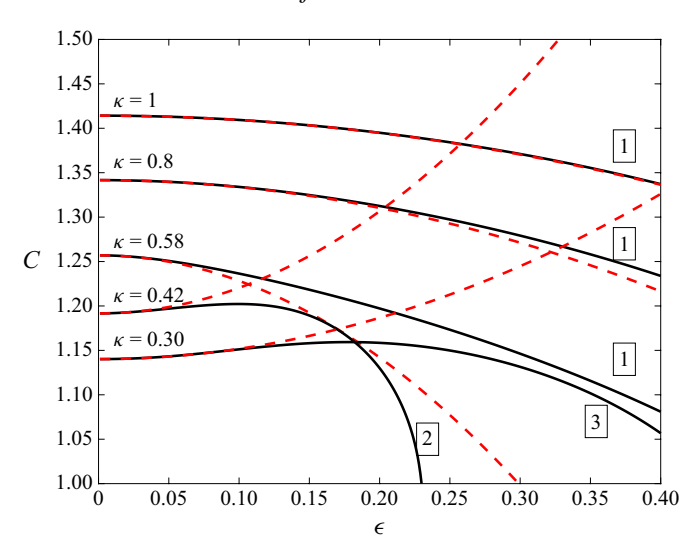


Figure 5. Plot of phase velocity C against ϵ for $\mu = 10$, $\Omega = 0$ and some values of $\kappa = 1.0, 0.80, 0.58, 0.42, 0.30$ (from top to bottom): solid lines show the numerical results, dashed lines the analytical results and the boxed number indicates the type of the waves.

difficulty, we take μ and κ as constants on a branch of solutions and vary Ω and ϵ over their admissible range in most of the cases studied here.

4.2. Gravity-capillary waves in irrotational flows

We first study irrotational flows with $\mu=10$ and several values of κ . The values $\kappa=1$ and 0.8 are taken to verify the correctness of the analytical solutions for GC waves, in which the effects of both gravity and capillarity are equally important, whereas the values of $\kappa=0.58,\ 0.42$ and 0.30 are used to determine the behaviour of the weakly nonlinear solutions close to the critical wavenumbers.

The variations of phase velocity C as a function of ϵ for $\Omega=0$ and several values of κ are shown in figure 5. The solid lines represent the numerical solutions of the Euler equations, and the dashed lines correspond to the approximate solutions. According to the asymptotic theory, the phase velocity decreases with the increase of ϵ for $\kappa=1$, 0.8 and 0.58 much like pure capillary waves, whereas it increases with ϵ for $\kappa=0.42$ and 0.30 much like pure gravity waves. For $\kappa=1$ and 0.8 the approximate solution agrees fairly well with the exact numerical solution over the range of ϵ values shown here. In contrast, with $\kappa=0.58$, 0.42 and 0.30 the approximate solution matches the exact solution only for small values of the amplitude parameter ϵ .

To better understand the meaning of the curves in figure 5, it should be realized that in general there is no unique branch of solutions for a fixed κ , in the neighbourhood or not of the critical wavenumbers. This was demonstrated numerically by the seminal work of Schwartz & Vanden-Broeck (1979) in the deep-water case. With our numerical method and continuation in either the amplitude parameter ϵ or the surface tension parameter κ , we find that this is also the case in finite depth, as illustrated by figure 6 where the variations of the squared phase velocity C^2 with κ are shown.

In this figure three branches of numerical solutions with $\mu=10$ and $\epsilon=0.10$ are plotted with solid lines, as well as the corresponding weakly nonlinear solution (dash–dotted line obtained with (B11)) and the linear solutions for infinitesimal waves with (dimensional) wavenumber nk_0 for n=1, 2 and 3 (dashed lines obtained with (3.5)). According to

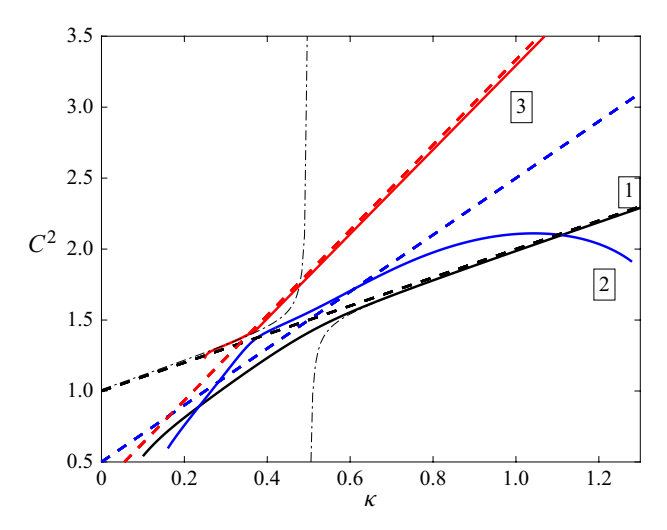


Figure 6. Plot of C^2 against κ for $\mu=10$, $\epsilon=0.10$ and $\Omega=0$. Solid line, numerical solutions; dash-dotted line, weakly nonlinear analytical solution; dashed lines, infinitesimal wave solutions.

the classification of the different branches of solutions proposed in Schwartz & Vanden-Broeck (1979), the types 1, 2 and 3 are represented in this figure, and correspond to the number of observed 'dimples' or inflexion points on a (half-) wave profile. Like in the deep-water case, for much of the figure the type number is seen to increase with C^2 for given κ . For this value of the amplitude parameter, $\epsilon=0.10$, the branches of types 1 and 3 follow the linear solution closely as κ increases from the critical values κ_1 and κ_2 , respectively, whereas the wave profiles become indistinguishable from a sinusoid with wavenumbers 1 and 3 (in units of k_0), respectively. In contrast, the branch of type 2 reaches a limiting configuration, as κ increases, through the trapping of a bubble (not shown). As $\kappa < \kappa_1$ decreases, all the branches reach a limiting configuration through the trapping of one or more bubbles (not shown). As expected, the approximate solution for C^2 , the dashdotted line in figure 6, breaks down as κ approaches the critical value κ_1 . An interesting feature of this curve, however, is that for decreasing values of $\kappa < \kappa_1$ it approaches first the branch of type 2, and matches almost perfectly the branch of type 3 when $0.25 < \kappa < 0.38$.

Knowing that initialization of the numerical continuation method with the linear solution with κ in the open intervals $[\kappa_1, \infty]$ and $[\kappa_n, \kappa_{n-1}]$ (with $n \ge 2$) yields numerical solutions corresponding to the branch of type n, one can realize that, in figure 5, the branches with $\kappa = 1$, 0.8 and 0.58 correspond to waves of type 1, while the branches with $\kappa = 0.42$ and 0.30 correspond to waves of the type 2 and 3, respectively. This analysis is supported by the examination of typical surface profiles for several values of ϵ and κ , as shown in figures 7 and 8.

Figure 7 shows that the trough becomes deeper and narrower as κ decreases from 1 to 0.8 and ϵ increases from 0.1 to 0.3. It is to be noted that it displays only wave profiles corresponding to the type 1. For these waves where surface tension balances gravity, we observe that the fourth-order analytical solution provides better results than the third-order solution for predictions of the surface elevation and is in good agreement with the exact numerical solution when $\epsilon \leq 0.2$.

Figure 8 shows for smaller values of ϵ the surface profiles of near resonant waves with $\kappa = 0.58$, 0.42 and 0.30. For waves with $\kappa = 0.58$, figure 8(a) shows that the troughs tend to sharpen with the increase of ϵ , whereas the crests tend to flatten, which is typical of

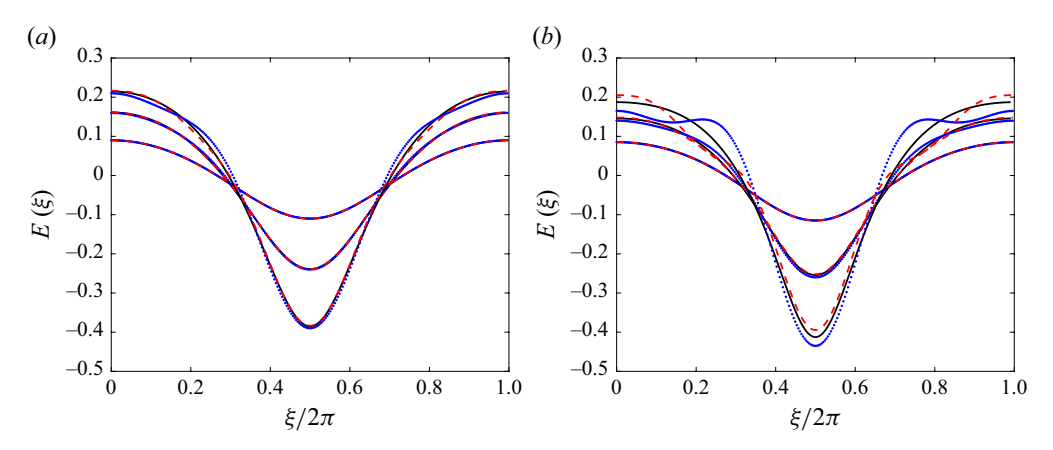


Figure 7. Comparison of surface profiles between third-order (dotted line), fourth-order (dashed line) and exact numerical solutions (solid line) for $\Omega = 0$, $\mu = 10$ and some values of $\epsilon = 0.3$, 0.2, 0.1 (from top to bottom); $(a) \kappa = 1$, $(b) \kappa = 0.8$.

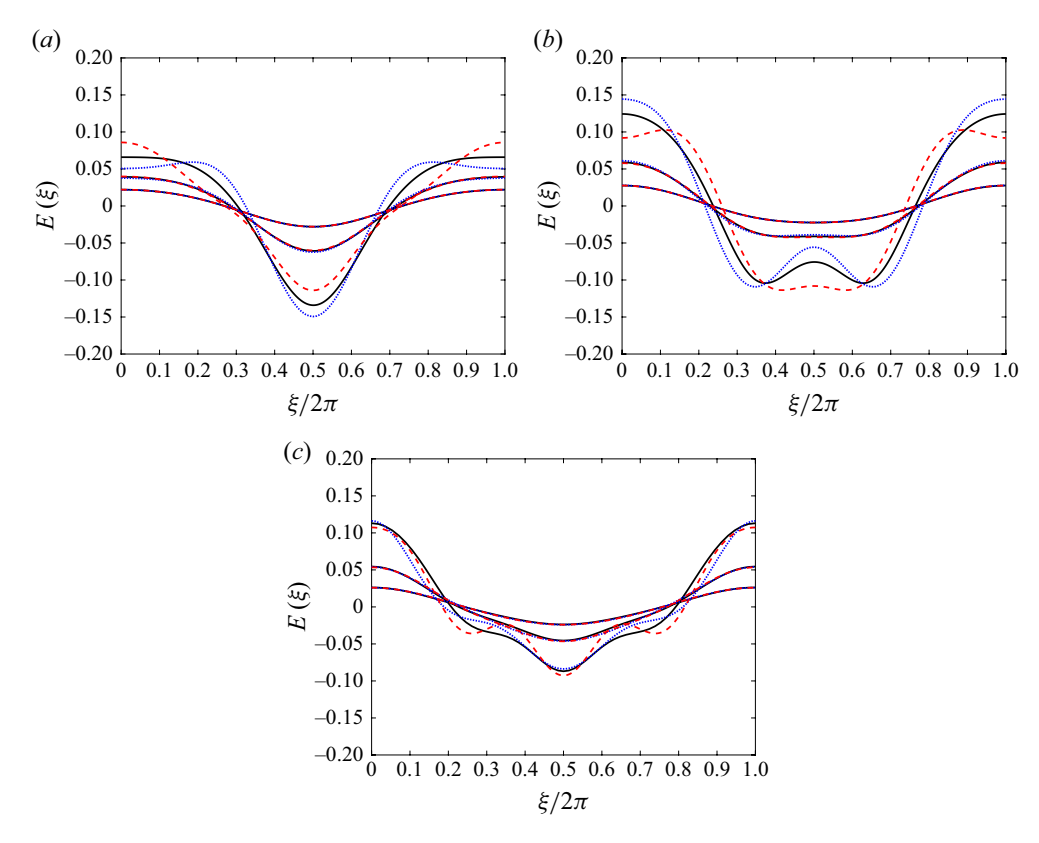


Figure 8. Comparison of surface profiles between third-order (dotted line), fourth-order (dashed line) and exact numerical solutions (solid line) for $\Omega=0$, $\mu=10$ and some values of $\epsilon=0.1, 0.05, 0.025$ (from top to bottom); (a) $\kappa=0.58$, (b) $\kappa=0.42$, (c) $\kappa=0.30$.

the waves of type 1. For the largest amplitude, $\epsilon = 0.1$, it is observed that the fourth-order solution makes a somewhat better job than the third-order solution, in the sense that it does not predict the formation of a crest dimple. Quantitatively, however, there is no significant improvement, neither near the crest nor near the trough. For waves with

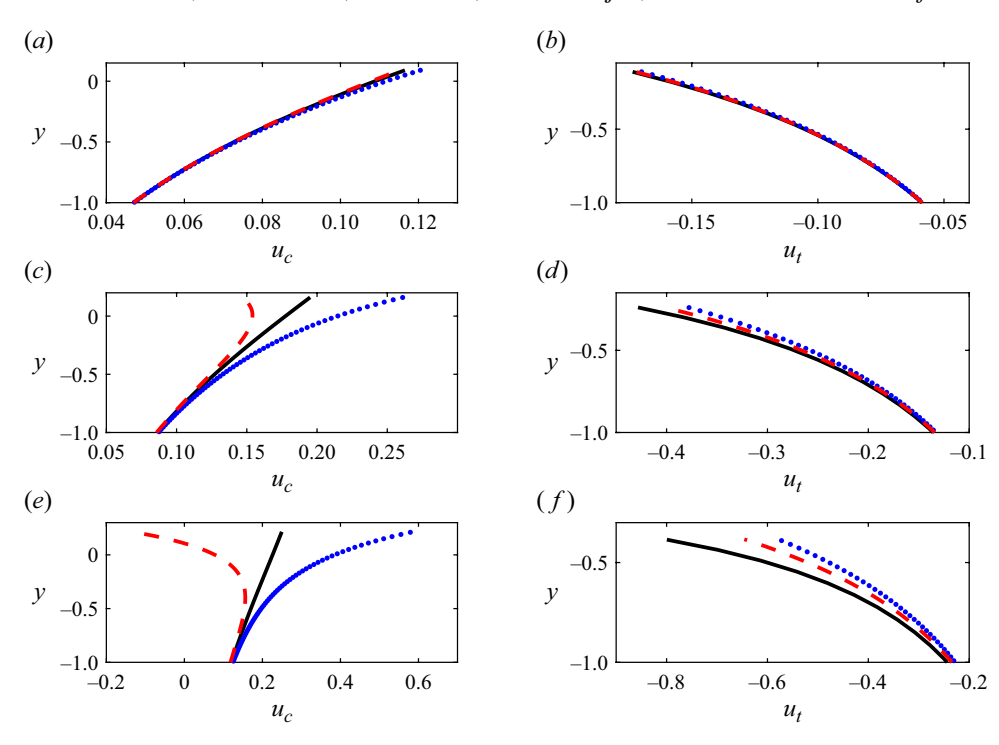


Figure 9. Comparison of horizontal velocity profiles between third-order (dotted line), fourth-order (dashed line) and exact numerical solutions (solid line) for the waves plotted in figure 7(a). The profiles beneath the crest are plotted in (a), (c) and (e), and beneath the trough in (b), (d) and (f); and the steepness increases as (a,b) $\epsilon=0.1$, (c,d) $\epsilon=0.2$ and (e,f) $\epsilon=0.3$.

 $\kappa=0.42$ the numerical solution indicates the presence of a secondary maximum on the surface profile with a trough between the two maxima, which is typical of the waves of type 2 (see figure 8b). For the largest amplitude, $\epsilon=0.1$, neither of the asymptotic solutions is in agreement with the numerical solution. In fact, the fourth-order solution incorrectly predicts the occurrence of a crest dimple that is absent in the profiles of the third-order and numerical solutions. With $\kappa=0.30$, the plots of figure 8(c) show that when the amplitude increases, the numerical solution takes the appearance of a primary sine wave with a relatively small 3-cycle perturbation superimposed upon it, which is typical of the waves of type 3. Similarly, neither of the asymptotic solutions is in agreement with the numerical solution for the largest amplitude considered here, though they predict qualitatively waves of type 3. It is noteworthy that when κ is close to κ_1 , like in figures 8(a) and 8(b), the fourth-order approximations fail more importantly than the third-order ones for the larger steepness, due to the fact that the associated small divisors in (3.13)–(3.17) are found to be squared in the fourth-order coefficients.

For further insight into the differences between the third- and fourth-order solutions, we have also compared the predictions of the interior flow with the numerical solutions. The method for the computation of the interior flow is explained in Ribeiro *et al.* (2017) and, therefore, need not be detailed here. To illustrate the differences in the interior flow, we have focused on the wave-induced horizontal velocities beneath the crest and the trough of the waves plotted in figure 7(a), where $\kappa=1$ is not close to κ_1 and $\epsilon=0.1$, 0.2 and 0.3. Figure 9 shows the comparison between the asymptotic solutions and the exact results

over the dimensionless range y = -1 to the free surface. Note that the bottom is located at y = -10, where the wave-induced velocities vanish (not shown).

For the smallest steepness, it is found that the fourth-order predictions are closer to the exact results both beneath the crest and the trough. However, for the larger steepness the differences between the third-order and the fourth-order are much more important beneath the crest than beneath the trough. Actually, below the trough it is observed that those differences increase with the steepness and the fourth-order predictions are closer to the exact results. Beneath the crest, those differences also increase with the steepness, but neither such approximations are close to the exact results in the near surface region. Nonetheless, as the depth increases the fourth-order solutions are found to be better than the third-order ones. These results can be explained, noting that, firstly the local slopes at the trough are in closer agreement with the exact results than they are the crest, and secondly that a binomial expansion has been used in the dynamic boundary condition to approximate the nonlinear term related to the surface tension. Only two terms in this binomial expansion are required for the third-order approximation, but three terms are necessary for the fourth-order approximation. Due to this approximation there is a mismatch between the approximate wave-induced horizontal velocities and the exact results, though the differences in the phase velocity are very small over the range of steepness considered here (see figure 5, the case $\kappa = 1$).

4.3. Gravity-capillary waves in flows with constant vorticity

Like in the previous subsection, we start by analysing the nonlinear dependency of the phase velocity on the wave steepness for the same different values of κ but with different values of the vorticity parameter Ω . According to the numerical solutions the dependency of C on ϵ is strongly affected by the vorticity whatever the value of κ , as shown in figure 10. In comparison with the case of irrotational flow (see figure 5), not only the values of C in the small amplitude limit are modified, but also the type of the waves depending on the value of κ . In figure 10 the solid lines represent the numerical solutions of the Euler equations, and the dashed lines correspond to the approximate nonlinear dispersion relation presented in § 3. As expected from the linear dispersion relation (3.5), it is observed that in the limit of small amplitude increasing negative vorticity ($\Omega > 0$) reduces the phase velocity, whereas increasing positive vorticity enhances it. In this limit the analytical results are in excellent agreement with the exact results whatever the value of κ .

When $\Omega>0$, figures 10(a) and 10(b) show that for each value of κ , the phase velocity is a decreasing function of the steepness. Except for the two lowest values of κ , namely 0.30 and 0.42, the agreement between the asymptotic theory and the exact theory is excellent over the range of steepness considered here, namely $0<\epsilon\leq0.25$. In any case, the exact results, as well as the corresponding approximations, show that the phase velocity is a decreasing function of steepness. This suggests that the waves are capillary-like. For the calculations with $\kappa=0.30$ and 0.42, it appears that the mismatch between the approximations and the exact results is reduced with the increase of Ω , the curves becoming closer to each other over a larger range of steepness. In contrast, when $\Omega<0$ the phase velocity is an increasing function of steepness for all κ values, except for the branch of solutions with $\kappa=1$ and $\Omega=-0.5$ that is plotted as shown in figure 10(c). In this figure, the exact branches of solutions with $\kappa=1$ and 0.8 agree with the approximations only when $\kappa<0.1$. In figure 10(d), $\Omega=-0.9$ and the agreement between the approximations and the exact results is very satisfactory over the range of steepness shown here, namely $0<\kappa\leq0.25$.

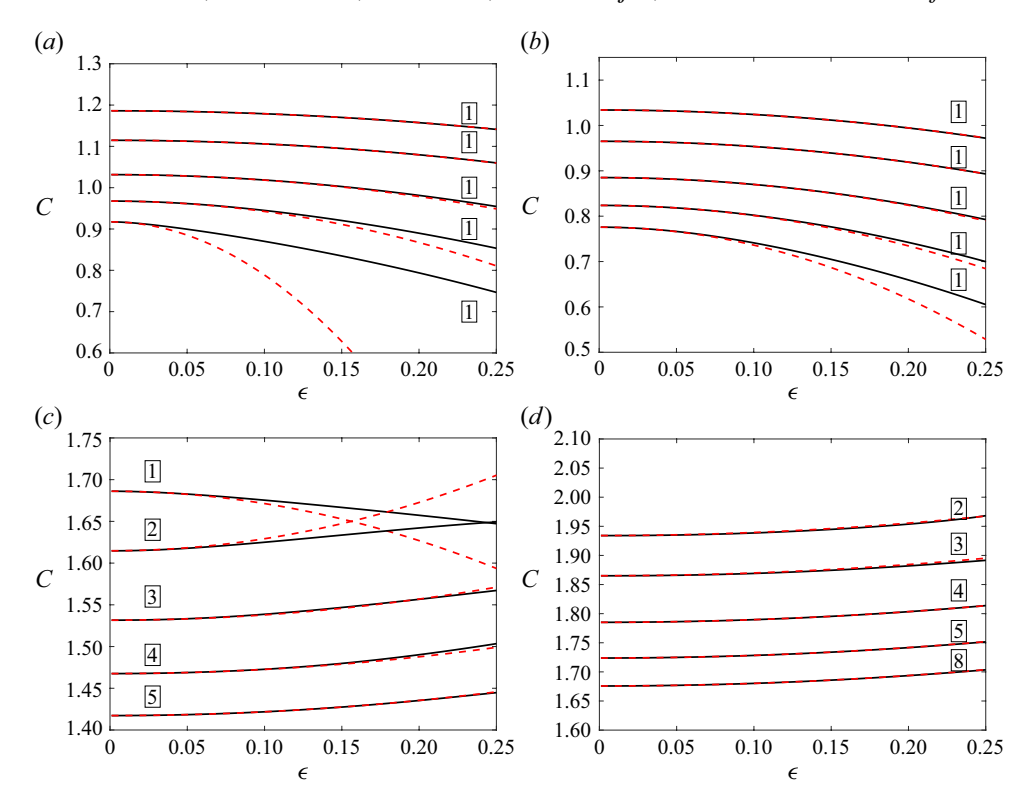


Figure 10. Plot of phase velocity C against ϵ for $\mu = 10$ and some values of $\kappa = 1.0, 0.80, 0.58, 0.42, 0.30$ (from top to bottom): solid lines show the numerical results, dashed lines the analytical results and the boxed number indicates the type of the waves; (a) $\Omega = 0.5$, (b) $\Omega = 0.9$, (c) $\Omega = -0.5$ and (d) $\Omega = -0.9$.

To identify the type of waves for each branch of solutions plotted in figure 10 we may adopt the reasoning used in § 4.2 for the GC waves in irrotational flows. This in turn requires us to determine the critical values of κ for given values of the intrinsic parameters \tilde{h} and $\tilde{\Omega}$. In our case $\mu=10$ and we have seen in § 3.2 that these critical values are mainly affected by the vorticity, the depth effects being negligible when $\tilde{h}\gg\tilde{h}_*$. For each value of κ and Ω used in figure 10, we have computed the first height κ_n . These values are reported in table 1. It should be emphasized that for given values of μ and μ 0, the intrinsic parameters \tilde{h} and $\tilde{\Omega}$ have different values that depend on the value of κ . The last column of table 1 indicates the type of the branch of solution for each triplet (μ, κ, Ω) considered in figure 10. Solutions are of type n+1 when the values of κ 1 falls in the interval $[\kappa_{n+1}, \kappa_n]$ for $n \geqslant 1$. Waves of type 1 have wavelengths such that $\kappa > \kappa_1$, where κ_1 is the largest critical wavenumber.

For several values of κ and a fixed wave steepness, $\epsilon=0.10$, we have also compared the surface profiles and the wave-induced horizontal velocities in the presence of a linear shear current with $\mu=10$. Figure 11 shows the comparison between the analytical solutions and the exact results for waves of different wavelengths, namely $\kappa=1,\ 0.80,\ 0.58,\ 0.42$ and 0.30, and a vorticity parameter $\Omega=0.5$. According to table 1 all the waves are of type 1, since their wavelength is such that $\kappa>\kappa_1$. Except for the longest wave with $\kappa=0.30$, there is a remarkable agreement between the analytical results and the exact ones, the fourth-order results being more accurate than the third-order ones. As expected, neither such approximations is valid for the waves with $\kappa=0.30$, a value that is very close to $\kappa_1\approx0.27$.

κ	Ω	$ ilde{h}$	$ ilde{\Omega}$	κ_1	κ_2	κ_3	κ_4	κ_5	κ_6	κ_7	κ_8	type
1.00	0.50	10.00	0.50	0.21	0.13	0.09	0.07	0.06	0.05	0.04	0.03	1
	0.90		0.90	0.08	0.05	0.03	0.02	0.02	0.01	0.01	0.01	1
	-0.50		-0.50	0.92	0.63	0.48	0.39	0.33	0.29	0.26	0.23	1
	-0.90		-0.90	1.34	0.92	0.71	0.59	0.50	0.44	0.39	0.36	2
0.80	0.50	11.18	0.47	0.22	0.14	0.10	0.08	0.06	0.05	0.04	0.04	1
	0.90		0.85	0.09	0.06	0.04	0.03	0.02	0.02	0.01	0.01	1
	-0.50		-0.47	0.90	0.61	0.47	0.38	0.32	0.28	0.25	0.23	2
	-0.90		-0.85	1.28	0.88	0.68	0.56	0.48	0.42	0.37	0.34	3
0.58	0.50	13.13	0.44	0.24	0.15	0.11	0.08	0.07	0.06	0.05	0.04	1
	0.90		0.79	0.11	0.07	0.05	0.03	0.03	0.02	0.02	0.01	1
	-0.50		-0.44	0.86	0.59	0.45	0.37	0.31	0.27	0.24	0.22	3
	-0.90		-0.79	1.21	0.83	0.64	0.53	0.45	0.39	0.35	0.32	4
0.42	0.50	15.43	0.40	0.25	0.16	0.12	0.09	0.07	0.06	0.05	0.05	1
	0.90		0.72	0.13	0.08	0.05	0.04	0.03	0.03	0.02	0.02	1
	-0.50		-0.40	0.83	0.57	0.43	0.35	0.30	0.26	0.23	0.21	4
	-0.90		-0.72	1.15	0.79	0.61	0.50	0.42	0.37	0.33	0.30	5
0.30	0.50	18.26	0.37	0.27	0.17	0.13	0.10	0.08	0.07	0.06	0.05	1
	0.90		0.67	0.14	0.09	0.06	0.05	0.04	0.03	0.03	0.02	1
	-0.50		-0.37	0.80	0.55	0.42	0.34	0.29	0.25	0.22	0.20	5
	-0.90		-0.67	1.09	0.75	0.57	0.47	0.40	0.35	0.31	0.28	8

Table 1. Values of \tilde{h} and $\tilde{\Omega}$ for given values of κ and Ω . Here $\mu = 10$ for each wave. The deep-water values of the first eight critical κ_n are also reported, as well as the type of each wave.

The same comparison has been carried out with $\Omega=-0.5$, and the results are shown in figure 12. According to table 1, each wave is of a different type. The type number is seen to increase with increasing wavelength. The shortest wave ($\kappa=1$) is the only capillary-like wave, in the sense that it belongs to a branch of solutions with decreasing phase velocity with increasing steepness (see figure 10c), and it is of type 1 as shown in figure 12(a). Again, for this value of κ that is close to the $\kappa_1\approx 0.92$, both the third-order and fourth-order solutions differ significantly from the exact results, the disagreement being larger near the crest than near the trough. For the wave of type 2 shown in figure 12(b) we have $\kappa=0.80$, which falls near the middle of the interval $[\kappa_2, \kappa_1]=[0.61, 0.90]$. Looking at the wave-induced horizontal velocities, it is found that the fourth-order theory does a better job than the third-order one beneath the trough, and that the situation is reversed beneath the crest. Nonetheless, both analytical solutions fail to match with the exact results in the near surface region. Actually, these differences between the exact results and the approximations are expected in view of figure 10(c), which shows that there is mismatch in the prediction of C for the waves with $\kappa=1$ and 0.80.

In contrast, for the gravity-like waves with $\kappa=0.58,\ 0.42$ and 0.30, figure 10(c) shows an excellent agreement between the exact phase velocity and the approximate one when $\epsilon=0.1$. Not surprisingly, when the value of κ is close to one of the first three critical values κ_n , both approximations fail to reproduce the near surface horizontal velocities (see figures 12c and 12d). However, when $\kappa=0.42$ we have $|\kappa-\kappa_2|=0.15,\ |\kappa-\kappa_3|=0.01,$ and although the approximate surface profiles are almost indistinguishable from the exact solution, it is found that there are important differences in the internal flow structure. Figure 12(d) shows that the fourth-order theory does a better job than the third-order one beneath the trough, the situation being reversed beneath the crest. As shown in figure 12(e), the surface profiles and the wave-induced horizontal velocities are indistinguishable from the exact solution for the wave with $\kappa=0.32$, which is in the interval $[\kappa_5, \kappa_4]$ and far enough the smallest critical value of either the third-order or fourth-order approximations.

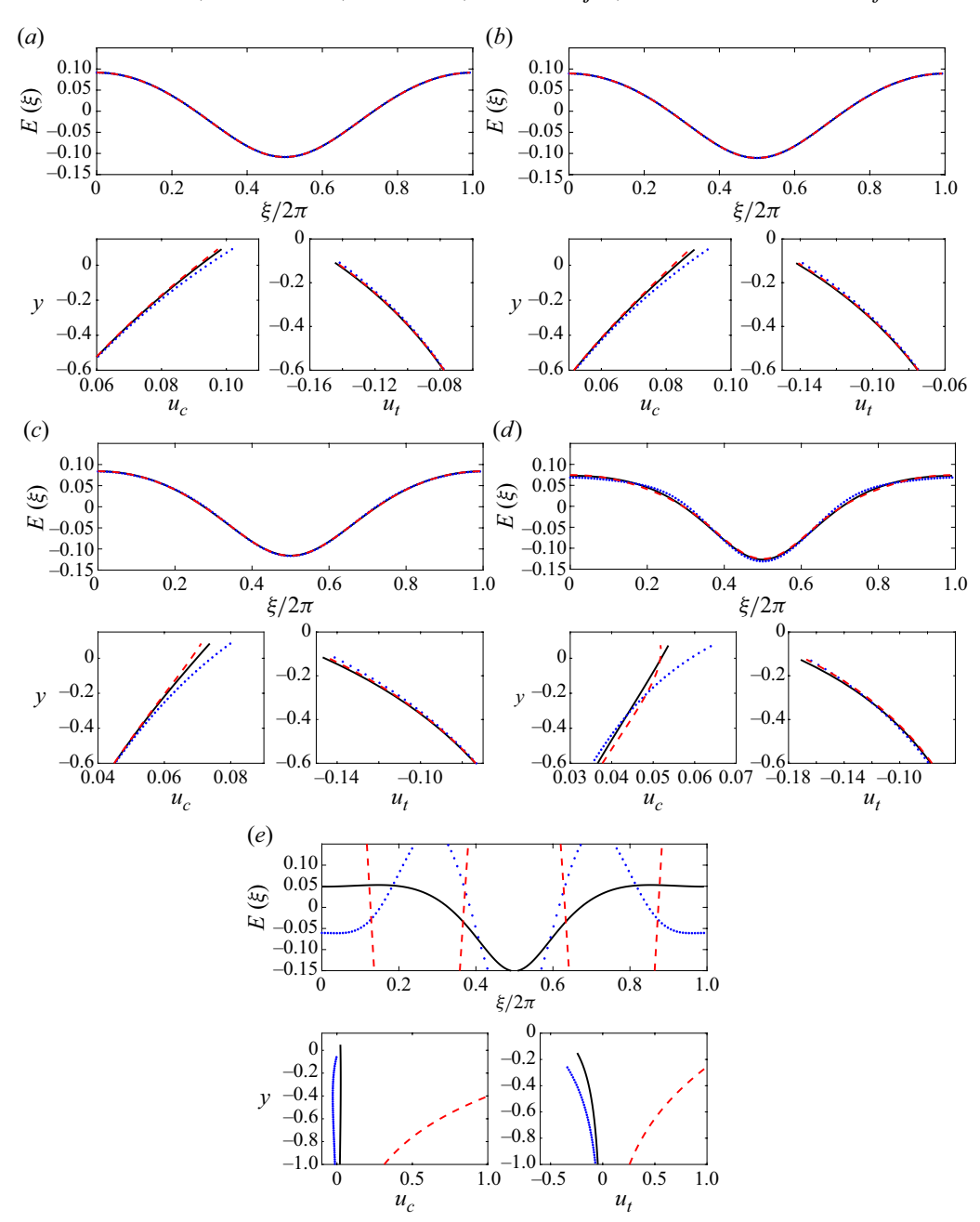


Figure 11. Comparison of surface profiles and wave-induced horizontal velocity profiles under crest (u_c) and trough (u_t) for waves with $\mu=10,~\Omega=0.5,~\epsilon=0.10$ and several values of κ . Third-order solution (dotted line), fourth-order solution (dashed line) and numerical solution (solid line): $(a)~\kappa=1$; $(b)~\kappa=0.80$; $(c)~\kappa=0.58$; $(d)~\kappa=0.42$; $(e)~\kappa=0.30$.

Finally we present the results of a similar comparison for steeper waves with $\mu=10,\ \Omega=\pm0.5$ and $\epsilon=0.2$. The four different waves have been chosen so that the approximation of the phase velocity is still in very good agreement with the exact solution. In view of the results of figures 10(a) and 10(c), we consider $\kappa=1$ and $\kappa=0.8$ with $\Omega=0.5$, whereas with $\Omega=-0.5$ we choose $\kappa=0.42$ and $\kappa=0.30$. For the waves with

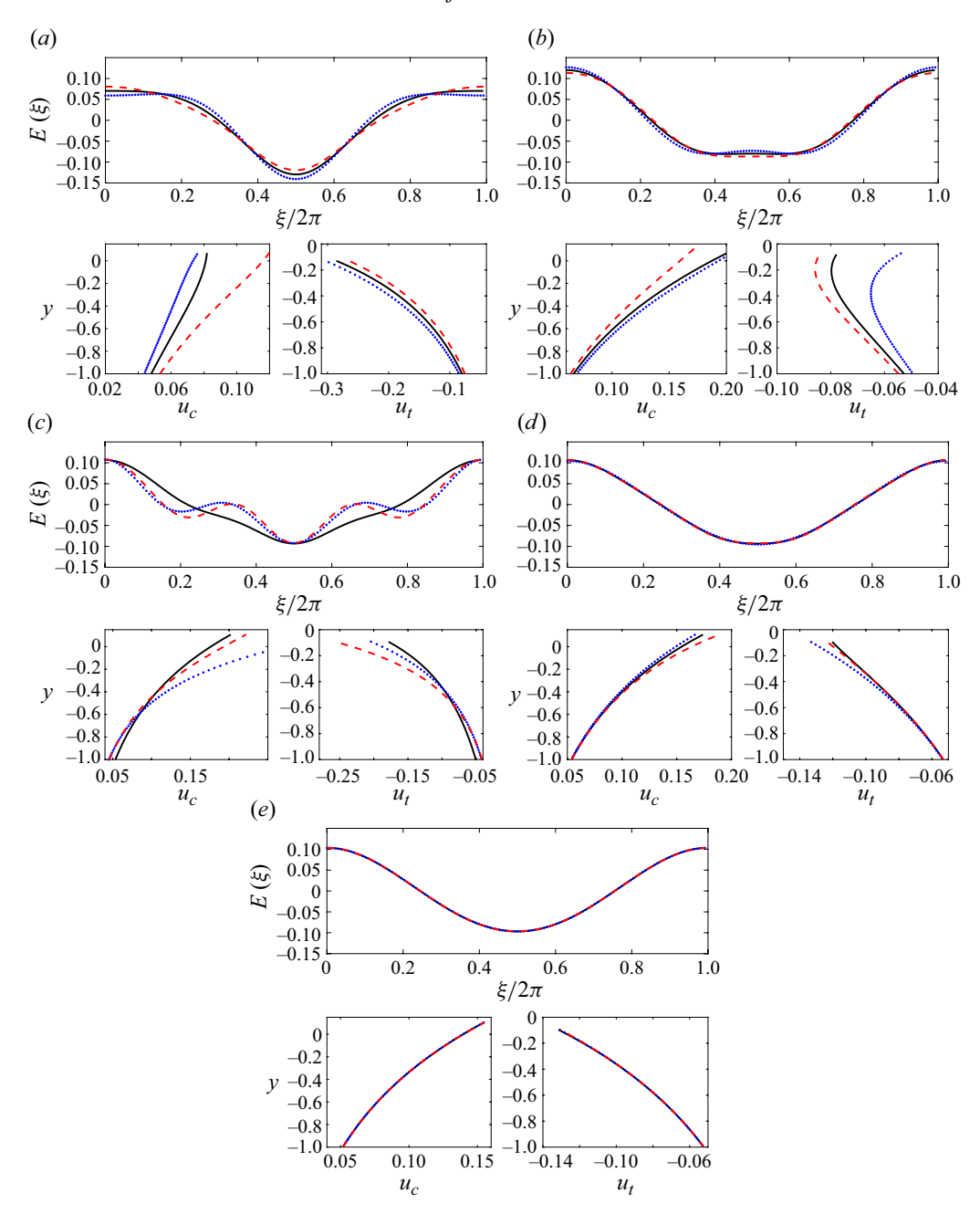


Figure 12. Same legend as in figure 11 but with $\Omega = -0.5$.

 $\Omega = 0.5$, κ is quite far from the first critical value κ_1 , and we observe that the thirdand fourth-order surface profiles are almost indistinguishable from the exact solution. However, in each case the approximations fail to describe the wave-induced velocities close to the surface. Nonetheless it should be noticed that the fourth-order solution performs better than the third-order one, though this improvement is lessened beneath the crest. For the waves with $\Omega = -0.5$ and $\kappa = 0.42$, which falls in $[\kappa_4, \kappa_3] = [0.35, 0.43]$,

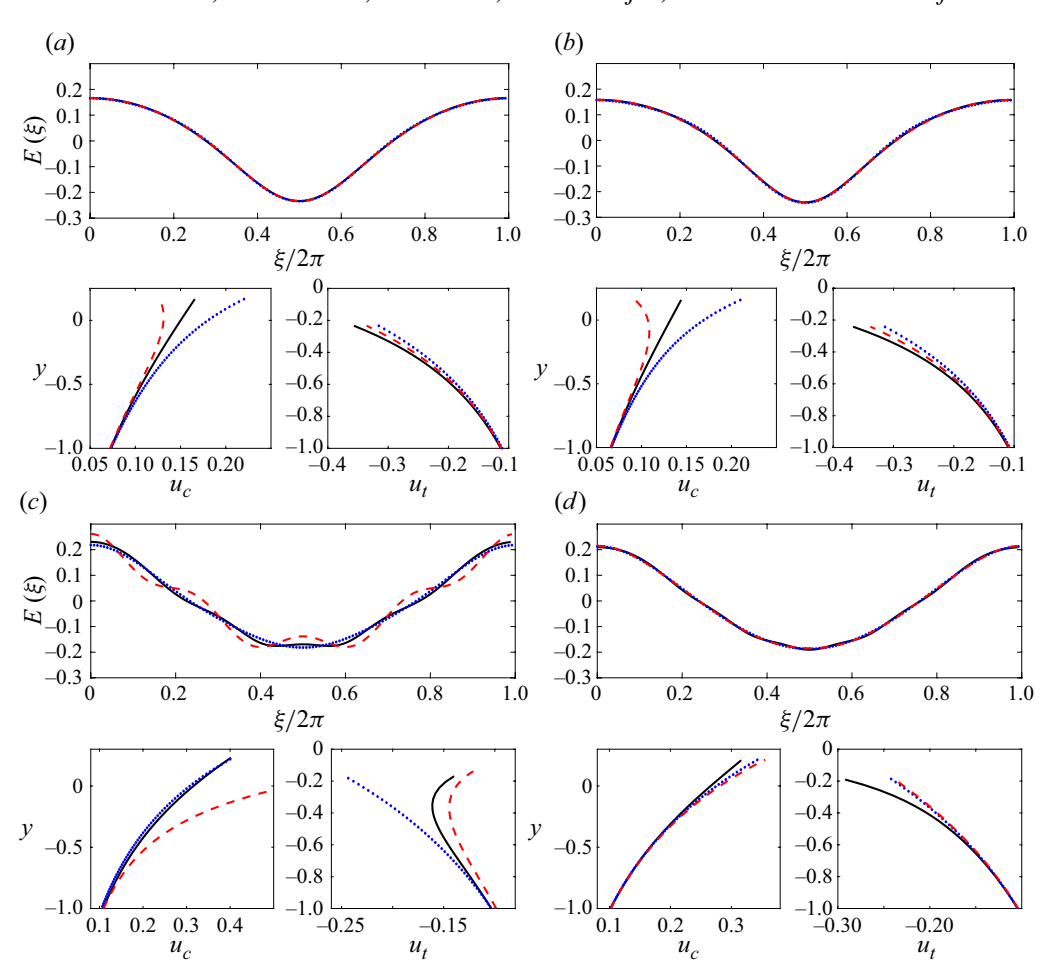


Figure 13. Comparison of surface profiles and wave-induced horizontal velocity profiles under crest (u_c) and trough (u_t) for waves with $\mu=10$, $\epsilon=0.20$. Third-order solution (dotted line), fourth-order solution (dashed line) and numerical solution (solid line): $(a) \kappa=1$, $\Omega=0.5$; $(b) \kappa=0.80$, $\Omega=0.5$; $(c) \kappa=0.42$, $\Omega=-0.5$; $(d) \kappa=0.30$, $\Omega=-0.5$.

figure 13(c) shows that nonlinearity has become sufficiently important to reveal the defect of the fourth-order theory in comparison with the third-order theory and the exact results (see also for comparison figure 12d). For the longest wave with $\kappa=0.30$, shown in figure 13(d), the approximate surface profiles are in very good agreement with the exact results. In this case the coefficients of the asymptotic series are well ordered, κ being $O(\epsilon)$ far from $\kappa_1=0.80$, $\kappa_2=0.55$ and $\kappa_3=0.42$, though they fail to predict the wave-induced velocities close to the surface beneath both crest and trough. Actually there is no improvement using the fourth-order theory and its results are very similar to that obtained with the third-order theory.

5. Conclusion

In this paper we have derived a fourth-order asymptotic solution for weakly nonlinear GC waves with constant vorticity in finite depth, and thereby, the works of Barakat & Houston (1968) and Hsu *et al.* (2016) have been extended.

We have shown that the determination of the critical values in the perturbation scheme, κ_n (for any $n\geqslant 1$), should be done with two intrinsic dimensionless parameters \tilde{h} and $\tilde{\Omega}$. It is emphasized here that, in the presence of surface tension, using instead μ and Ω may be misleading in the study of the effects of both vorticity and depth on the occurrence of these critical wavenumbers. We have found that vorticity changes the critical depth \tilde{h}_* , below which no resonances are possible and, thus, the perturbation scheme is valid for any wavelength specified with κ . This critical depth increases without bound with increasing positive values of $\tilde{\Omega}$ (negative vorticity). In contrast it decreases slowly with increasing positive vorticity.

To test the accuracy of the third-order and fourth-order solutions, we have used a numerical method of solution based on a truncated Fourier series approximation in a conformal formulation of the problem. The fourth-order results are interesting as they reveal important differences not only in the surface profiles but also in the internal flow structure, when compared with the third-order predictions. With negative vorticity $(\Omega > 0)$, the fourth-order solution improves on the third-order solution, inasmuch as the steepness is relatively small and the dimensionless squared wavenumber is far enough the first three critical values. With positive vorticity $(\Omega < 0)$, the outcome of the comparison between the third and fourth order is rather surprising. Our analysis reveals that there are important differences in the wave-induced velocities below the free surface, even though the predicted surface profiles as well as phase velocities are in good agreement with the numerical solutions.

Finally, we point out that we have not tested the approximations in the shallow water limit, $\mu \ll 1$. We merely recall that without vorticity the classical Stokes expansion method become less accurate when both the amplitude ϵ and the Ursell number ϵ/μ^3 significantly increases. This usually implies a severe restriction on the steepness when moving to shallow water. How this restriction is affected, as vorticity effects become important in the presence of surface tension, remains to be explored.

Acknowledgements. This work was started during a visit by Professor A.K. Dhar to the University of Turin, Italy. During this work, Professor Dhar was supported by a CPDA grant from the IIEST, Shibpur under grant no. 1593/D(FW)/22. The award of the Senior Research Fellowship (ref. no. 276/ACAD/2023) by the IIEST, Shibpur to S. Halder is gratefully acknowledged. We thank the anonymous referees for their valuable comments, which helped us improve the quality of this manuscript.

Declaration of interests. The authors report no conflict of interest.

Appendix A. Approximate solution of the second order

Equating the second power of ϵ , we have the following sequence of equations:

$$\Phi_{2\xi\xi} + \Phi_{2\eta\eta} = 0, \quad -\mu \leqslant \eta < 0,$$

$$\Phi_{2\eta} + C_0 E_{2\xi} = -E_1 \Phi_{1\eta\eta}$$

$$+ (\Phi_{1\xi} + \Omega E_1 - C_1) E_{1\xi}, \quad \eta = 0,$$

$$C_0 \Phi_{2\xi} - (1 - C_0 \Omega) E_2 + \kappa E_{2\xi\xi} = \frac{1}{2} (\Phi_{1\xi}^2 + \Phi_{1\eta}^2)$$

$$+ \frac{1}{2} \Omega^2 E_1^2 + \Omega \Phi_{1\xi} E_1 - C_0 E_1 \Phi_{1\xi\eta}$$

$$- C_1 (\Phi_{1\xi} + \Omega E_1) - \frac{1}{2} K_2, \quad \eta = 0,$$

$$\Phi_{2\eta} = 0, \quad \eta = -\mu.$$
(A1)

Terms depending on η appearing in equations for $\eta = 0$, as $E_1(\xi)\Phi_{1\eta\eta}$ and $E_1(\xi)\Phi_{1\xi\eta}$ are obtained by using Taylor series expansion given by

$$\Phi(\xi, \eta) \approx [\Phi(\xi, \eta)]_{\eta = E} + E(\xi)[\Phi(\xi, \eta)_{\eta}]_{\eta = E} + E^{2}(\xi)[\Phi(\xi, \eta)_{\eta\eta}/2]_{\eta = E}.$$
 (A5)

Using the second-order Laplace equation (A1) and the boundary condition (A4) we obtain the expressions for second-order potential and surface elevation in a similar way

$$\Phi_2(\xi, \eta) = A_2 \frac{\cosh[2(\eta + \mu)]}{\cosh(2\mu)} \sin(2\xi),$$
(A6)

$$E_2(\xi) = a_2 \cos(2\xi).$$
 (A7)

Using (A6)–(A7) and the first-order solutions in the boundary conditions (A2)–(A3), we get the coefficients as follows:

$$A_2 = \frac{C_0 \epsilon^2 (1 + \sigma^2)}{8(1 - 3\overline{\kappa})\sigma^4} [\overline{\Omega}^2 + 3(1 + \overline{\Omega}) + 3\sigma^2 (\overline{\kappa}\overline{\Omega} + 2\overline{\kappa} - 1)], \tag{A8}$$

$$a_2 = \frac{\epsilon^2}{4(1 - 3\overline{\kappa})\sigma^3} [\overline{\Omega}^2 + 3(1 + \overline{\Omega}) - \sigma^2(1 - \overline{\Omega})], \tag{A9}$$

$$K_2 = \frac{C_0^2 \epsilon^2}{2\sigma^2} [(1 + \overline{\Omega})^2 - \sigma^2],$$
 (A10)

$$C_1 = 0. (A11)$$

Classically, the nonlinear correction of the phase velocity is unknown at this order and must be determined at the next order.

As found by Hsu *et al.* (2016), the expressions of A_2 and a_2 given by (A8) and (A9) are found to be singular when κ equals κ_1 , given implicitly as the root of the following equation:

$$\kappa = \frac{\sigma^2}{(3 - \sigma^2) + 3\overline{\Omega}}.$$
(A12)

Without vorticity ($\overline{\Omega} = 0$), (A12) reduces to the expressions obtained by Barakat & Houston (1968) and Djordjevic & Redekopp (1977). In deep water ($\sigma = 1$) without vorticity, it further reduces to the well-known value $\kappa_1 = 1/2$.

Appendix B. Approximate solution of the third order

To derive the third-order approximate solution, we proceed in a similar manner and obtain the following sequence of equations:

$$\Phi_{3\xi\xi} + \Phi_{3\eta\eta} = 0, \quad -\mu \leqslant \eta < 0, \tag{B1}$$

$$\Phi_{3\eta} + C_0 E_{3\xi} = -E_1 \Phi_{2\eta\eta} - E_2 \Phi_{1\eta\eta} - \frac{1}{2} E_1^2 \Phi_{1\eta\eta\eta} + (\Phi_{1\xi} + \Omega E_1) E_{2\xi} + (\Phi_{2\xi} + E_1 \Phi_{1\xi\eta} + \Omega E_2 - C_2) E_{1\xi}, \quad \eta = 0, \tag{B2}$$

$$C_0 \Phi_{3\xi} - (1 - C_0 \Omega) E_3 + \kappa E_{3\xi\xi} = -C_0 \left(E_1 \Phi_{2\xi\eta} + E_2 \Phi_{1\xi\eta} + \frac{1}{2} E_1^2 \Phi_{1\xi\eta\eta} \right) + (\Phi_{1\xi} + \Omega E_1) (\Phi_{2\xi} + E_1 \Phi_{1\xi\eta} + \Omega E_2 - C_2) + \Phi_{1\eta} (\Phi_{2\eta} + E_1 \Phi_{1\eta\eta}) + \frac{3}{2} \kappa E_{1\xi\xi} E_{1\xi}^2 - \frac{1}{2} K_3, \quad \eta = 0, \tag{B3}$$

$$\Phi_{3\eta} = 0, \quad \eta = -\mu. \tag{B4}$$

Solving (B1)–(B4) we get the expressions for velocity potential and surface elevation amplitude as follows:

$$\Phi_3(\xi, \eta) = A_{33} \frac{\cosh[3(\eta + \mu)]}{\cosh(3\mu)} \sin(3\xi) + A_{31} \frac{\cosh[(\eta + \mu)]}{\cosh(\mu)} \sin(\xi)$$
 (B5)

$$E_3(\xi) = a_{33}\cos(3\xi) + a_{31}\cos(\xi). \tag{B6}$$

The derivation for obtaining the following results involves some algebra. On substituting (B5)–(B6) and using the first and second-order solutions into the boundary conditions (B2–B3), we obtain

$$A_{33} = \frac{C_{0}\epsilon^{3}}{64(1-3\overline{\kappa})\left[1-\overline{\kappa}(3+\sigma^{2})\right]} \frac{(1+3\sigma^{2})}{\sigma^{7}} \left[\overline{\Omega}^{4} + \left\{2(3+\sigma^{2})+8\overline{\kappa}\sigma^{2}\right\}\overline{\Omega}^{3} + \left\{(15-\sigma^{2})+\overline{\kappa}\sigma^{2}(43+19\sigma^{2})\right\}\overline{\Omega}^{2} + \left\{(15-\sigma^{2})+\overline{\kappa}\sigma^{2}(43+19\sigma^{2})\right\}\overline{\Omega}^{2} + \left\{2(9-8\sigma^{2}-\sigma^{4})+12\overline{\kappa}\sigma^{2}(7+\sigma^{2})+24\overline{\kappa}^{2}\sigma^{4}(1+\sigma^{2})\right\}\overline{\Omega} + (9-22\sigma^{2}+13\sigma^{4})+\overline{\kappa}\sigma^{2}(60-32\sigma^{2}-13\sigma^{4})+3\overline{\kappa}^{2}\sigma^{4}(16+5\sigma^{2})\right], \quad (B7)$$

$$A_{31} = \frac{C_{2}\epsilon^{3}}{\sigma} + \frac{C_{0}}{\sigma}a_{31} - \frac{C_{0}\epsilon^{3}}{8(1-3\overline{\kappa})}\frac{1}{\sigma^{5}}\left[\overline{\Omega}^{3} + (5+2\sigma^{2})\overline{\Omega}^{2} + \left\{3(3+\sigma^{2})+3\overline{\kappa}\sigma^{2}(1+\sigma^{2})\right\}\overline{\Omega} + (6-\sigma^{2})+3\overline{\kappa}\sigma^{2}(2-\sigma^{2})\right], \quad (B8)$$

$$a_{33} = -a_{31} = \frac{\tanh(3\mu)}{C_{0}}A_{33} + \frac{\epsilon^{3}}{8(1-3\overline{\kappa})}\frac{1}{\sigma^{4}}\left[\overline{\Omega}^{3} + (5+2\sigma^{2})\overline{\Omega}^{2} + \left\{3(3+\sigma^{2})+3\overline{\kappa}\sigma^{2}(1+\sigma^{2})\right\}\overline{\Omega} + (6-\sigma^{2}-2\sigma^{4})+3\overline{\kappa}\sigma^{2}(2+\sigma^{2})\right], \quad (B9)$$

$$K_{3} = 0, \quad (B10)$$

$$C_{2} = \frac{C_{0}}{8(\overline{\Omega}+2)(1-3\overline{\kappa})}\frac{1}{\sigma^{4}}\left[\overline{\Omega}^{4} + 2(3+\sigma^{2})\overline{\Omega}^{3} + \left\{3(5+\sigma^{2})+3\overline{\kappa}\sigma^{2}(1+\sigma^{2})\right\}\overline{\Omega}^{2} + \left\{2(9-2\sigma^{2}+\sigma^{4})+12\overline{\kappa}\sigma^{2}(1-\sigma^{2})\right\}\overline{\Omega} + (9-10\sigma^{2}+9\sigma^{4}) + 3\overline{\kappa}\sigma^{2}(4-8\sigma^{2}-\sigma^{4})+9\overline{\kappa}^{2}\sigma^{6}\right]. \quad (B11)$$

At third-order approximation the first non-vanishing nonlinear correction of the phase velocity C_2 is given by (B11) that matches (3.32) of Hsu *et al.* (2016), who first obtained this analytical result. The expressions for the third-order terms in (B7) and (B9) are found to be singular when κ equals κ_2 , given implicitly as the root of the following equation:

$$\kappa = \frac{\sigma^2}{3(1+\overline{\Omega}) + \sigma^2 \overline{\Omega}}.$$
 (B12)

Taking $\overline{\Omega} = 0$ in (B12) yields $\kappa_2 = \sigma^2/3$, in agreement with the results of Barakat & Houston (1968). In deep water $\sigma = 1$ and we obtain the other well-known value $\kappa_2 = 1/3$.

REFERENCES

BARAKAT, R. & HOUSTON, A. 1968 Nonlinear periodic capillary-gravity waves on a fluid of finite depth. J. Geophys. Res. 73 (20), 6545–6554.

Brantenberg, C. & Brevik, I. 1993 Higher order water waves in currents of uniform vorticity, in the presence of surface tension. *Physica Scripta* 47 (3), 383–393.

- CHABANE, M. & CHOI, W. 2019 On resonant interactions of gravity-capillary waves without energy exchange. Stud. Appl. Maths 142 (4), 528–550.
- CHOI, W. 2009 Nonlinear surface waves interacting with a linear shear current. Maths Comput. Simul. 80 (1), 29–36.
- CURTIS, C.W., CARTER, J.D. & KALISCH, H. 2018 Particle paths in nonlinear Schrödinger models in the presence of linear shear currents. *J. Fluid Mech.* **855**, 322–350.
- DHAR, A.K. & KIRBY, J.T. 2023 Fourth-order stability analysis for capillary-gravity waves on finite-depth currents with constant vorticity. *Phys. Fluids* **35** (2), 026601.
- DJORDJEVIC, V. & REDEKOPP, L.G. 1977 On two-dimensional packets of capillary-gravity waves. J. Fluid Mech. 79 (4), 703–714.
- FANG, H., LIU, P.L.-F., TANG, L. & LIN, P. 2023 The theory of fifth-order stokes waves in a linear shear current. *Proc. R. Soc. A* 479 (2280), 20230565.
- GAO, T., MILEWSKI, P.A. & WANG, Z. 2021 Capillary-gravity solitary waves on water of finite depth interacting with a linear shear current. *Stud. Appl. Maths* **147** (3), 1–22.
- GUO, D., TAO, B. & ZENG, X. 2014 On the dynamics of two-dimensional capillary-gravity solitary waves with a linear shear current. *Adv. Math. Phys.* v. 2014 480670, 1–7.
- HARRISON, W.J. 1909 The influence of viscosity and capillarity on waves of finite amplitude. Proc. Lond. Math. Soc. 2 (1), 107–121.
- HOGAN, S.J. 1980 Some effects of surface tension on steep water waves. Part 2. J. Fluid Mech. 96 (3), 417–445.
- HOGAN, S.J. 1981 Some effects of surface tension on steep water waves. Part 3. J. Fluid Mech. 110, 381–410.
- HSU, H.C., FRANCIUS, M., MONTALVO, P. & KHARIF, C. 2016 Gravity-capillary waves in finite depth on flows of constant vorticity. *Proc. R. Soc. Lond. A* 472 (2195), 20160363.
- HSU, H.C., KHARIF, C., ABID, M. & CHEN, Y.Y. 2018 A nonlinear Schrödinger equation for gravity—capillary water waves on arbitrary depth with constant vorticity. Part 1. *J. Fluid Mech.* **854**, 146–163.
- HUR, V.M. 2019 Shallow water models with constant vorticity. Eur. J. Mech. (B/ Fluids) 73, 170–179.
- HUR, V.M. & JOHNSON, M.A. 2015 Modulational instability in the Whitham equation with surface tension and vorticity. *Nonlinear Anal.* **129**, 104–118.
- IVANOV, R.I. & MARTIN, C.I. 2019 On the time-evolution of resonant triads in rotational capillary-gravity water waves. *Phys. Fluids* **31** (11), 117103.
- KANG, Y. & VANDEN-BROECK, J.M. 2000 Gravity-capillary waves in the presence of constant vorticity. *Eur. J. Mech. (B/ Fluids)* **19** (2), 253–268.
- MARTIN, C.I. & MATIOC, B.-V. 2013 Existence of wilton ripples for water waves with constant vorticity and capillary effects. *SIAM J. Appl. Maths* **73** (4), 1582–1595.
- MARTIN, C.I. 2013 Local bifurcation and regularity for steady periodic capillary–gravity water waves with constant vorticity. *Nonlinear Anal. Real World Appl.* **14** (1), 131–149.
- NAYFEH, A.H. 1970a Finite amplitude surface waves in a liquid layer. J. Fluid Mech. 40 (4), 671–684.
- NAYFEH, A.H. 1970b Triple- and Quintuple-Dimpled Wave Profiles in Deep Water. *Phys. Fluids* 13 (3), 545–550.
- PIERSON, W.J. & FIFE, P. 1961 Some nonlinear properties of long-crested periodic waves with lengths near 2.44 centimeters. *J. Geophys. Res.* **66** (1), 163–179.
- RIBEIRO, R., MILEWSKI, P.A. & NACHBIN, A. 2017 Flow structure beneath rotational water waves with stagnation points. *J. Fluid Mech.* **812**, 792–814.
- SCHWARTZ, L.W. 1974 Computer extension and analytic continuation of Stokes' expansion for gravity waves. J. Fluid Mech. 62 (3), 553–578.
- SCHWARTZ, L.W. & VANDEN-BROECK, J.M. 1979 Numerical solution of the exact equations for capillary—gravity waves. *J. Fluid Mech.* **95** (1), 119–139.
- SHELTON, J., MILEWSKI, P.A. & TRINH, P.H. 2021 On the structure of steady parasitic gravity-capillary waves in the small surface tension limit. *J. Fluid Mech.* 922, A16.
- WILTON, J.R. 1915 Lxxii. on ripples. Lond. Edin. Dublin Phil. Mag. J. Sci. 29 (173), 688-700.